Accepted Manuscript

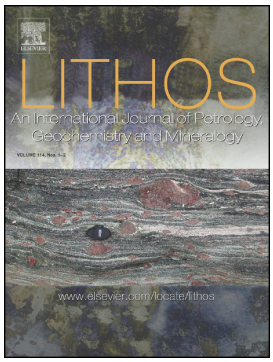

Insights into orogenic processes from drab schists and minor intrusions: Southern São Francisco Craton, Brazil

Hugo Moreira, Lucas Cassino, Cristiano Lana, Craig Storey, Capucine Albert

PII: S0024-4937(19)30297-X
DOI: https://doi.org/10.1016/j.lithos.2019.07.013
Reference: LITHOS 5146

To appear in: *LITHOS*

Received date: 12 April 2019
Accepted date: 12 July 2019

Please cite this article as: H. Moreira, L. Cassino, C. Lana, et al., Insights into orogenic processes from drab schists and minor intrusions: Southern São Francisco Craton, Brazil, LITHOS, https://doi.org/10.1016/j.lithos.2019.07.013

Insights into orogenic processes from drab schists and minor intrusions: Southern São Francisco Craton, Brazil

Hugo Moreira[a], Lucas Cassino[b], Cristiano Lana[b], Craig Storey[a], Capucine Albert[b,c]

[a] School of Earth and Environmental Sciences, University of Portsmouth, Burnaby Building, Burnaby road, Portsmouth, PO1 3QL, UK;

[b] Applied Isotope Research Group, Departamento de Geologia, Escola de Minas, Universidade Federal de Ouro Preto, Ouro Preto, MG 35400-000, Brazil;

[c] Department of Earth Sciences, University of Cambridge, Downing Street, Cambridge CB2 3EQ, UK

Abstract

Minor altered intrusions and drab retrogressed schists can easily be overlooked in geological studies but this contribution explores these rocks within the Archaean and Palaeoproterozoic southern São Francisco Craton (SSFC), Brazil using geological relationships and accessory mineral in situ analyses in the context of cratonic assembly. Three magmatic pulses are documented: i) Archaean and ii) Palaeoproterozoic felsic intrusions, both hosted by Archaean protoliths, and iii) Palaeoproterozoic felsic intrusions in Palaeoproterozoic supracrustal sequences. Archaean felsic intrusions confirm the Palaeoarchaean age of the mafic/ultramafic sequence of the Rio das Velhas Greenstone Belt and Rhyacian intrusions mark the collisional stage of the Mineiro Belt with the SFC at c. 2130 Ma. Greenstone belt schists show a wide distribution of rounded 'soccer ball' Archaean detrital and metamorphic zircon grains ranging in age from 3200 to 2750 Ma with an interpreted overprinting high-grade metamorphic event at c. 2700 to 2680 Ma. Most high-grade metamorphic rims have Th/U > 0.1, negative $\varepsilon Hf_{(t)}$ values and REE pattern consistent with eclogite/granulite metamorphic facies, reinforcing the hypothesis of a dehydrated-refractory crust formed during the stabilization of the SSFC, even though no such protoliths are preserved. This event links crustal thickening and partial melting of Archaean lower crust. Archaean rutile crystals from the greenstone belt schist were reset during the Palaeoproterozoic event but still preserve the early Archaean high-grade metamorphic signature. The presence of unstable ilmenite replaced by rutile in the schist, associated to felsic intrusions with the same age at c. 2130 Ma suggest high pressure, low temperature prograde metamorphism during the collisional stage of the Palaeoproterozoic orogen. Elongate and prismatic zircon grains from the Rhyacian intrusions have low $\varepsilon Hf_{(t)}$ signature and crystallised from partial melting of sedimentary protoliths. Accretionary events produced thicker and more differentiated crust by the end of Rhyacian time. Easily overlooked rocks in this study, when studied, have revealed a rich multi-event history of cratonic evolution.

Keywords: Petrochronology; Accessory minerals; Felsic intrusions; Granulites; São Francisco Craton; Crustal differentiation

Introduction

Geological research in collisional orogens tends to emphasize major geological units, intrusions, main tectonic features and metamorphic complexity revealed by phase relationships and their chemistry. Adjacent accreted terranes are sites of major crustal reworking, recording information about lithospheric evolution and continental crust development (Bickle, 1986; Kusky and Polat 1999; Jaupart and Mareschal, 2015; Polat et al., 2015; Kamber, 2015). While fundamental, these types of topics often fail to discover more cryptic features that can be hidden or are difficult to reveal. At the same time, minor intrusions at outcrop scale, highly retrogressed rocks, and complex local structures are often under-studied or perceived to have dubious larger scale orogenic importance. We investigate just these types of rocks in this study to determine what they might reveal in relation to an orogen's evolution.

Robust accessory mineral phases are fundamental tools in this study as they are resistant against most of the alteration and deformation processes during retrograde metamorphism and weathering of the host rock. Moreover, they can be useful tracers of orogenic processes due to their unique geochemical characteristics, such as radiogenic isotopes and/or trace element composition. This is particularly important for ancient terranes, because as they have experienced multiple episodes of deformation, they potentially preserve much of the early history often lost in the incomplete geological record.

The cratonic margins around the paleo- southern São Francisco Craton (SSFC), are particularly useful areas to address the questions presented above. They are punctuated by a combination of crust- and mantle-derived rocks, which provide important information about the tectonic history of the ancient parts of the continental crust and the surrounding accreted terranes (e.g., Alkmim and Teixeira, 2017 and references therein) (Fig. 1a, b). Despite recent geochronology/geochemistry studies on the Archaean basement (Romano et al. 2013; Lana et al., 2013; Farina et al., 2015; Albert et al., 2016) and on the 2470 - 2100 Ma surrounding orogenic rocks, known as the Minas accretionary orogeny (Seixas et al., 2012; 2013; Ávila et

al., 2014; Teixeira et al., 2015; Barbosa et al., 2015; Barbosa et al 2018; Moreira et al., 2018), the currently available geochronological and isotopic datasets from the margins of the SSFC are not sufficiently detailed to fully constrain the nature of amalgamation and magmatism that took place during tectonic accretion around its margins.

The ancient crust in the SSFC exhibits a dome-and-keel architecture potentially formed in the Archaean and reactivated during the Palaeoproterozoic (Marshak et al., 1997; Cutts et al., 2019). It was assembled and stabilised in the Archaean (Romano et al., 2013; Lana et al 2013), and enlarged to the east and south through a prolonged period of tectonic accretion and arc-related magmatism in the Palaeoproterozoic (Aguilar et al., 2017; Heilbron et al., 2017; Alkmim and Teixeira, 2017). This accretion and reactivation of the dome-and-keel structure is linked to the well-known Palaeproterozoic orogeny in South America, and is often considered to represent part of the amalgamation of the SSFC (Alkmim and Marshak 1998).

Lithological units involved in tectonic amalgamation are preserved in the southern margins of the craton and record the Archaean tectonic history and Palaeoproterozoic syn-to post-collisional magmatic events (Fig. 1b). They comprise imbricated slices of Archaean greenstone belt rocks (Rio das Velhas Supergroup) and Palaeoproterozoic clastic sandstones (Fig. 2a), and are enclosed between the Bação and Santa Rita Domes (Fig 2a; b). They are also marked by multiple injections of small-scale felsic intrusions that are interpreted to be related to partial melting during the doming event (e.g., Alkmim and Marshak 1998) or to the Palaeoproterozoic magmatic arc to the south – The Mineiro Belt (MB) (Fig 1a; b). Such igneous rocks may hold the key to the timing of important events in the region, including the early history of greenstone belt sequences in the SSFC as well as the timing of deformation during the SSFC-MB collision. These intrusions can either represent a window to sources at depth or be sourced locally from partial melting of the surrounding rocks. Ultimately, the interaction between stable continental blocks and surrounding magmatism plausibly clarifies the overall crustal resilience of Archaean cratonic areas during tectonic activity (Kamber, 2015; Hawkesworth et al., 2016; Reimink et al., 2016).

In this paper, we address several questions, namely: (1) the extent of Archaean magmatism within the SSFC, (2) the timing of docking of the MB against the SSFC, (3) the age of the Rio das Velhas Greenstone belt within the SSFC, and (4) the age and source rocks of granitoids, crustal residence and relationship to crustal components in this area of Precambrian Brazilian rocks. The methods we use are primarily U-Pb zircon and rutile ages, Lu-Hf isotopes and trace element composition from felsic intrusions and their host rocks in the Rio das Velhas and Minas supergroups, in the context of known geological relationships. We also draw on published U-Pb-Hf and whole rock Sm-Nd analyses of the surrounding Mineiro Belt rocks to assess magmatic sources. As the greenstone belt schists appear to have experienced high grade metamorphism, we carefully assess ages and textures along with trace elements, Ti – thermometry within zircon grains and Zr – thermometry in rutile crystals to shed light on the characteristics of the metamorphic overprint.

Background

The geological history of the SSFC may be divided into two stages. The first stage follows a classic Archaean granite-greenstone belt evolution (from 3220 to 2680 Ma), encompassing TTG-like magmatism and contemporaneous extrusion of greenstone mafic and ultramafic volcanic rocks of the Nova Lima Group, the main unit of the Rio das Velhas Supergroup (Baltazar and Zucchetti, 2007; Machado and Carneiro, 1992; Romano et al., 2013; Teixeira et al., 1996). The second stage has been interpreted as a 'modern-style' Wilson cycle that took place at the margins of the Archaean block between c. 2.6 and 2.0 Ga (Alkmim and Marshak, 1998) involving rifting, arc magmatism and subsequent collision (Fig. 2b).

The Archaean history of the SSFC began with a period of magmatic activity (3220 - 3200 Ma) and the construction of a Palaeoarchaean TTG nucleus, known as the Santa Bárbara complex, preserved in the eastern part of the region (Fig. 1). The second phase (2920 - 2850 Ma), known as the Rio das Velhas I (RV I) event, is recorded in the granitoid-gneiss

complexes in the region (Lana et al., 2013). Since this event seems responsible for the first development of continental lithosphere in the SSFC, it has been suggested that the mafic and ultramafic basal layers of the Rio das Velhas Supergroup may have formed at this time, in addition to other greenstone belt remnants in the region (da Fonseca et al., 2017; Verma et al., 2017). However, there is no direct geochronological or geological evidence for such a Mesoarchaean greenstone belt in or around the craton. The third, Rio das Velhas II (RV II), event (2800 - 2760 Ma) is interpreted as the result of magmatic arc activity around the margins of the Rio das Velhas-Santa Bárbara block (Lana et al., 2013). It also produced felsic volcanic rocks that occur within the Rio das Velhas Supergroup (Noce et al., 2005). The RV II event was followed shortly after by the emplacement of high-K granites, between 2760 and 2680 Ma, possibly in a collisional setting (referred to as Mamona event by Farina et al., 2015). These granites are distinct from the TTG-like magmas and are derived from partial melting of protoliths including metasedimentary rocks (Albert et al., 2016). This long period of igneous activity was coeval with the deposition of a thick clastic unit interpreted as a foredeep or foreland basin, the Maquiné Group (Moreira et al., 2016). Both the deposition of a thick sedimentary pile and the high-K magma production in a probable convergent to collisional context are thought to mark the transition out of Archaean-type geodynamics and the final stabilization of this crustal segment. However, the nature of this transitional period and the question whether subduction occurred is still a topic of debate.

In the Palaeoproterozoic, the Archaean crust of the SSFC was stretched and a major rift basin was opened, which later evolved into the passive margin of the Minas Basin (Alkmim and Marshak, 1998; Hartmann et al., 2006), one of the most economically important Precambrian basins in South America. The sedimentary record of the Minas Basin constitutes a approx. 8000 m-thick pile (the Minas Supergroup) representing the development of the passive margin and its subsequent inversion during the Rhyacian orogeny, as well as sedimentation related to the orogenic collapse, the Itacolomi Group (Alkmim and Martins-Neto, 2012). The rift and marine initiation phases of this basin are represented by the Tamanduá and Caraça Groups, quartz-rich metasandstones and conglomerates that grade to

black shales with minor carbonate rocks, the former being represented by the Moeda Formation and the latter by the Batatal Formation (Dorr 1969; Renger et al., 1995; Koglin et al., 2014; Martínez Dopico et al., 2017). The overlying Itabira Group is subdivided into the Cauê and the Gandarela formations. The first is composed of Lake Superior-type banded iron formation metamorphosed to itabirites, whereas the latter is composed of limestones and dolomites (Dorr, 1969; Babinski et al., 1995; Alkmim and Martins-Neto 2012). In turn, the overlying sedimentary sequence comprises a package of passive margin marine deposits (mostly quartzites and phyllites), the Piracicaba Group (Renger et al., 1995; Mendes et al., 2014). The beginning of tectonic instability is marked by the deposition of the overlying Sabará Group, composed of phyllites, tuffs, greywackes and diamictites (Dorr 1969; Reis et al., 2002). The regional unconformity between the Piracicaba and the Sabará groups represents a hiatus of c. 300 Ma and a change of sedimentation regime from passive margin to convergent setting has been interpreted as evidence for the inversion of the Minas Basin (Alkmim and Teixeira, 2017).

The southern and eastern borders of the SSFC are in tectonic contact with a composite continental arc built upon the cratonic margin (the Mantiqueira Complex) and with a juvenile terrane (the MB) (e.g., Heilbron et al., 2010; Teixeira et al., 2015; Aguilar et al. 2017).The juvenile terrane is interpreted as an elongate and relatively older island arc (Alkmim and Teixeira 2017). The igneous record of the c. 2.1 Ga Palaeoproterozoic orogeny starts from an extensive belt to the south of the SSFC dominated by 2350-2120 Ma juvenile granitoids of the MB (Seixas et al., 2012, 2013). The extension of island arcs into the northern section of the craton (Heilbron et al 2010; Aguilar et al., 2017), the absence of the continental arc between the MB and the SSFC, and evidence of ocean basin consumption have yet to be clearly documented. However, this area comprises Palaeoproterozoic oceanic and continental arcs juxtaposed with the Archaean basement by accretionary processes and final collision (Noce et al., 2000; Teixeira et al., 2015).

The Archaean–Palaeoproterozoic block was locally overprinted by metamorphism associated with the Neoproterozoic Brasiliano orogeny (c. 700 to 450 Ma) along the

southeastern margin of the craton (Chemale et al., 1994; Alkmim and Marshak, 1998). This was the last orogenic event that affected the province and therefore defines the present outline of the São Francisco Craton (Fig. 1a).

Rationale and metamorphic grade relationships

Elongate keels of supracrustal rocks and broad, kilometer-scale granitoid-gneiss domes characterize much of the eastern part of the SSFC, at the heart of the Quadrilátero Ferrífero (QF) mining district (e.g., Dorr 1969). Figure 2 shows the study area, in the southern margin of the Bação Complex, encompassing the Dom Bosco Syncline. It consists of an imbricate thrust system akin to a duplex structure (Fig. 2), within a canoe-shaped trough, filled by imbricated sediments of the Piracicaba, Sabará and Itacolomi groups. The southern limb of the syncline is bounded by an intercalation of the Rio das Velhas Supergroup and the Itacolomi Group sequences. The Ouro Branco mountain range is aligned with one of the isolated occurrences of the Itacolomi Group, essentially composed of erosional resistant meta-sandstones and meta-conglomerates. Its sigmoidal shape is delimited at the north and south by major sinistral strike-slip faults colinear with the Neoproterozoic Brasiliano E-W trend (Dorr, 1969; Alkmim and Marshak, 1998). The same trend is responsible for the imbrication of the layers within the syncline. The northern limb of the syncline is defined by the basal units of the Minas Supergroup, which in turn is topographically marked by the Ouro Preto mountain range. Further north, the antiformal structure containing the Ouro Preto mountain range as one of its limbs is named the Mariana Anticline. This anticline contains the Rio das Velhas Supergroup filling its core and its hinge plunges southeastward (Fig. 2). This area comprises, therefore, one of the several low-grade polydeformed surpracrustal sequences of the SSFC at its margins.

The supracrustal sequences experienced amphibolite facies with the highest grades adjacent to basement domes, but most of the Archaean and Palaeoproterozoic metasedimentary sequences have low greenschist facies metamorphic grade (partly due to

retrogression) (Fig. 1a). There is a regional increase of the metamorphism eastwards, and there are no reports of granulite facies rocks. Sporadic kyanite and other Al_2SiO_5 polymorphs are best described in the northwest portion of the SSFC (Jordt-Evangelista et al., 1992). The first metamorphic study trying to constrain the zones within the SSFC divided the area into 4 domains based on index metamorphic minerals (Herz, 1978). The grunerite-cummingtonite series was also used to define metamorphic domains (Pires, 1995) and later associated to tectonic deformation (Rosière and Chemale, 2000). High temperature – low pressure aureoles in contact with the basement domes (from Alkmim and Teixeira, 2017) and index metamorphic minerals (Herz, 1978) are shown in figure 1.

Small scale quartzo-feldspathic intrusions are present within metasedimentary rocks in this region and mostly located near the cratonic margins. They have variable dimensions, but most are between 1 to 3 m in length and 0.5 to 1 m in thickness. They comprise quartz and albite and can be foliated, usually sub-parallel to the host-rock foliation. Intrusion and host rocks appear to share some of the tectonic-metamorphic history, but some contacts can be interpreted as locally discordant to foliation (Fig. 3). In general, these intrusions are more prolific towards the boundary between the Archaean and Palaeoproterozoic terranes and close to regional thrust faults. Proximal to less prominent tectonic boundaries, the intrusions are not as numerous but are relatively thicker (Fig. 3e). Regardless of origin and outcrop scale characteristics, they can potentially provide insight to tectonic accretion processes in the Palaeoproterozoic.

Sampling

Locality A

Samples A1 and A2 (641430/7729758 - Fig. 2a) are felsic intrusions near the so-called Santa Rita dome (Alkmim and Marshak, 1998), a TTG-greenstone block bounded to the southwest by the NW-SE oriented Congonhas lineament, which marks the contact with the Mineiro Belt (Fig. 1b). The Dome is bounded to the north by the E-W oriented Engenho fault, which forms the contact with a major trough (the Dom Bosco syncline) containing supracrustal

rocks from the Rio das Velhas and Minas supergroups and from the Itacolomi Group (Fig. 2). The samples were collected from two intrusions hosted in Rio das Velhas Supergroup schists (Fig. 3a; c), one of the many greenstone-belt remnants of the Santa Rita dome. The two sampled intrusions, located 15 m from one another, are small (about 1 m in thickness), very altered quartz-feldspathic bodies, and stretched along the host-rock schistosity (e.g. Fig. 3c).

Locality B

Sampling site B (647050/ 7734681 – Fig. 2a) is located north of the Engenho fault, in the Dom Bosco syncline domain, therefore separated from locality A by an important regional discontinuity. It is situated within a approx. 30 km^2 occurrence of a schist-dominated sequence of the Rio das Velhas Supergroup, in thrust contact with metasedimentary rocks of the Itacolomi Group (that form the Ouro Branco ridge) and, in its northwestern limit, over metasedimentary rocks of the Minas Supergroup; its occurrence is delimited on its eastern side by overlapping metasedimentary rocks of the Itacolomi Group. The area has a roughly triangular shape and is informally named the Itatiaia block (Fig. 2a). The rocks are composed of mainly chlorite- and chlorite-quartz schist, with common epidote, white mica, biotite, hornblende, carbonate and plagioclase, the main accessory phases are rutile, zircon, magnetite and tourmaline. The sequence also includes quartzites, talc schists and some banded iron formations. The area is important for hosting the only gold deposit with massive to disseminated base-metal (Pb-Zn-Cu) sulfides of the QF. The deposit, mined in the 1940s, is known as Bico de Pedra mine and is located in the northernmost part of this occurrence of the Rio das Velhas Supergroup (Fig. 2a). Its sulfides are associated with carbonate-chlorite-talc-biotite schist (komatiitic peridotite) and carbonate-quartz-biotite-chlorite-plagioclase schist (basalt), as well as a quartzo-feldspathic intrusion (Vial et al., 2007). The eastern part of the area contains abundant granitoid magmatic injections of varied sizes, composed essentially of quartz, albite and some mica, most being oriented sub-parallel to the host-rock foliation. The intrusive bodies are sheared and sometimes folded and faulted, but the larger ones partly preserve phaneritic igneous textures (e.g. Fig. 3d). Three of these intrusions were sampled for zircon geochronology (labelled B2a, B2b and B2c) as well as the hosting epidote-chlorite-

quartz schist (B1a) (Fig. 3b; c). Sample B1a is in direct contact with sample B2a (647072/7734705) and approximately 150 m from samples B2b and B2c (646959/7734603), which in turn are only 10 m from each other. Intrusion B2a is better preserved, with granoblastic texture formed by plagioclase (~50%) up to 5 mm in length and quartz (ca. 30%) crystals surrounded by phyllosilicates. In thin section, sample B1a is composed of quartz (~40%), epidote (~25%), and chlorite (~30%). The remaining ~5% corresponds to the following accessory phases: magnetite, ilmenite, tourmaline, rutile and zircon. The schist is intensely foliated. Titanite is not present, but rutile is common, which ranges in size from a few microns to half mm in diameter and is generally porous and partially dissolved, although subhedral grains can be found. Zircon grains are aligned with the schistosity. Ilmenite is found as relict cores rimmed by rutile or as acicular inclusions. If the sample was at amphibolite facies or higher grade originally (as suggested by the presence of rutile), extensive retrogression has re-equilibrated to middle greenschist (epidote-biotite-chlorite) facies. Epidote is also present in the matrix and along with biotite, primary muscovite, rutile and zircon make up about 5% of the sample. Rutile grains comprise a trail that follows the main foliation, possibly caused by dissolution and recrystallisation. Detailed description of the thin sections as well as Scanning Electron Microscope - Energy Dispersive X-ray Spectroscopy (SEM-EDS) analyses of the mineral phases are presented in the supplementary material.

Locality C

Sample C1 (649435/7747255) was collected on the BR-356 highway margin near Ouro Preto. The highway runs roughly parallel to the Ouro Preto mountain ridge. The ridge represents the Dom Bosco syncline north limb and is composed of metasedimentary sequences of the Minas Supergroup. Sample C1 was collected from a structurally concordant body (approximately 2 m thick) within mica-quartz-feldspar schist interlayered with altered itabirite and dolomitic rocks that comprise the Cauê Formation (Fig. 2a; 3e, f). The foliation in the intrusive rocks, intense and parallel to the host rock schistosity, suggests that both were involved in the same deformation process (Fig. 3f).

Methodology

Collected samples were ~10 kg in weight and were submitted to usual comminution procedures by jaw crusher and disk mill facilities at the Universidade Federal de Ouro Preto (UFOP), Brazil. Heavy minerals were concentrated by panning and the magnetic fraction was split out using a rare earth element hand magnet. Zircon and rutile grains were picked using a Leica binocular stereoscopic microscope and mounted in epoxy resin. The mounts were polished exposing the internal section of the grains and imaged using a JEOL JSM-6510 Scanning Electron Microscope and collecting cathodoluminescence (CL) and Backscattered-electron (BSE) images to identify different compositional domains. In terms of U-Pb and Lu-Hf analyses in zircon grains, the first two U-Pb sessions and the Lu-Hf systematics were done at UFOP, as well as the first session of trace element analyses in rutile. Zircon trace element analyses and a third session of U-Pb analyses in zircon and rutile grains were done at the University of Portsmouth (UoP), UK.

U-Pb geochronology

Most U-Pb analyses in zircon grains were performed at UFOP during two sessions: the first one was carried out using an Agilent 7700x Quadrupole Inductively Coupled Plasma Mass Spectrometer (Q-ICP-MS) coupled to a 213 nm New Wave Nd:YAG laser (sample C1), while the second session was performed using a Thermo-Finnigan Element 2 Sector Field Inductively Coupled Plasma Mass Spectrometer (SF-ICP-MS) equipped with a CETAC213 laser ablation system (samples A1, A2, B1 and B2).

During the first session, laser ablation was performed using a 30 μm spot size, 6–8 J/cm^2 fluence and 10 Hz repetition rate. Ablations were carried out using He as a carrier gas mixed with Ar prior to introduction into the ICP-MS. Sequences consisted of 15 s of background measurement, 50 s of ablation signal acquisition and 15 s for washing out. Integration times were 15 ms for ^{206}Pb and ^{238}U, 40 ms for ^{207}Pb and 10 ms for ^{208}Pb, ^{204}Pb + ^{204}Hg and ^{232}Th. Detailed protocols for the U–Pb analyses are described in Takenaka et al. (2015). GJ-1 zircon (^{207}Pb/^{206}Pb age of 608 ± 1 Ma; Jackson et al., 2004) was used as primary

reference material and Plešovice zircon (337 ± 1 Ma; Sláma et al., 2008) was used for quality control, as a secondary standard.

In the second U-Pb session, each analysis was acquired using a 20 μm spot size after 20 seconds of background measurement and 20 s sample ablation. Laser repetition rate was 10 Hz and fluence was ~3.5 J/cm^2. Operating conditions were similar to those of Farina et al. (2015), Moreira et al. (2016) and Martínez Dopico et al. (2017). Mass bias was made using repeated measurements of GJ-1 zircon standard (Jackson et al., 2004) and the accuracy of the corrections was checked by measuring Blue Berry – BB9 zircon (562 ± 1 Ma; Santos et al., 2017) and M127 (524 ± 1 Ma; Nasdala et al., 1998) as secondary zircon standards. Zircon reference materials were alternately analyzed under the same conditions as the unknown zircon grains and yielded accurate results compared with their ID-TIMS ages with long term reproducibility of 1% (See supplementary data). Data were reduced using the *Glitter* software (van Achterbergh et al., 2001) and plotted in diagrams using the Excel *Isoplot v.3.0* program (Ludwig, 2003).

Complementary zircon U-Pb analyses were carried out on sample B1a at UoP using an Analytik Jena PlasmaQuant Elite ICP-MS coupled to an ASI RESOlution 193 nm ArF excimer Laser. Analyses were done with a 15 μm spot size, laser fluence was 2.5 J/cm^2 and a repetition rate of 2 Hz. There was 20 s of background measurement, followed by 30 s of ablation and 15 s of washout for each analysis. Three pulses of pre-ablation using a 20 μm spot size were used to clean the area before each analysis (after the cleaning there was a washout for 15 seconds). The run consisted of 3 analyses of the reference material and thereafter it was analysed once every 3-4 analyses of unknowns or secondary standards. BB9 zircon (Santos et al., 2017) was used as primary standard. Two other zircon reference materials were used as secondary standards to assess the accuracy and precision of the analytical run; Temora (ID-TIMS age of 416.75 ± 0.24 Ma; Black et al., 2003) and Plešovice zircon (Sláma et al., 2008). Additionally, zircon grains from the Kaap Valley tonalite were also dated (SHRIMP age of 3226 ± 14 Ma; e.g. Armstrong et al., 1990). The ages obtained do not

deviate more than 1% from the reference published values of the secondary standards, when treated as 'unknowns'.

U-Pb analyses in rutiles from sample B1a were performed in a single session at the University of Portsmouth also using the Analytik Jena PlasmaQuant Elite ICP-MS coupled to an ASI RESOlution 193 nm ArF excimer Laser. Analyses consisted of 40 µm spot size, laser fluency was 4.0 J/cm^2 and repetition rate was 5 Hz. Analyses consisted of 20 s of measured background, 30 s of ablation time and 15 s of wash-out. Before each analysis, three laser pulses of 45 µm spot size and the same ablation conditions were performed, followed by 20 s wash out in order to clean the rutile surface. Integration times were 10 ms for ^{202}Hg, ^{204}Pb, ^{208}Pb, ^{232}Th, ^{235}U and ^{238}U; 20 ms for ^{206}Pb and 30 ms for ^{207}Pb. R10 rutile (average ID TIMS age of 1091.3 ± 4.7 Ma, Luvizotto et al., 2009a) was used as primary standard and R13 (SIMS age of 504 ± 4 Ma; Schmitt and Zack, 2012), R19 (ID TIMS age of 493 ± 10; Zack et al., 2011) and in-house SAE standard (unpublished ID TIMS age of 495 Ma, C. Lana) rutiles were used as secondary standards. They yielded Concordia ages of 1092 ± 5 Ma, 476 ± 4 Ma, 499 ± 4 Ma and 497 ± 3 Ma, respectively. The ages are within 2% of published values for both primary and secondary standards, except for R13 (4%). Most of the grains have low common lead concentration and corrections (based on ^{204}Pb or ^{208}Pb), do not significantly change the overall age of the unknown rutiles, although the analyses devoid of common lead were used preferentially for age calculations and interpretation (see results and supplementary material).

Lu-Hf analysis

In situ zircon Lu-Hf analyses were carried out at UFOP using a Thermo-Finnigan Neptune multi-collector ICP-MS coupled to a Photon-Machines 193 nm excimer laser system. Most of the analyses were performed on top of previous 20 µm spot U-Pb analyses, in the same compositional domain, using a spot size of 40 µm and 6 Hz repetition rate during 36 s of static mode acquisition. A few grains with available areas of the same compositional domain had the Lu-Hf analyses performed right next to the previous U-Pb analyses, instead of on top of them. The analytical procedures described by Gerdes and Zeh (2006, 2009) have been

adopted. The isobaric interference of ^{176}Yb and ^{176}Lu on ^{176}Hf was corrected by measuring ^{173}Yb and ^{175}Lu isotopes and applying mass bias corrected natural ratios to subtract the interfering isotopes. The isotope ^{177}Hf was also measured and its typical signal was approximately 10 V. Analyses of the zircon standards Temora (Black et al., 2003; Wu et al., 2006), Mud Tank (Black and Gulson 1978; Woodhead and Hergt, 2005) and 91500 (Wiedenbeck et al., 1995) were performed before and after the sample analyses on pristine areas. Multiple analyses of these reference materials yielded average ^{176}Hf/^{177}Hf ratios of 0.282665 ± 15 (2SD, n = 2), 0.282506 ± 15 (2SD, n = 16) and 0.282298 ± 25 (2SD, n = 16), respectively. These measured ^{176}Hf/^{177}Hf are compatible with published data, ensuring accuracy. A detailed description of data acquisition is outlined by Albert et al. (2016).

Trace element analysis

Trace element composition of zircon and rutile grains from sample B1A was obtained in order to evaluate their crystallisation temperature and metamorphic facies, following the Ti-in-zircon and Zr-in-rutile thermometers (Watson et al., 2006; Ferry and Watson 2007). For the zircon grains, their REE pattern was also analysed (Rubatto, 2017).

Zircon analyses were conducted using an ASI RESOlution Excimer 193 nm laser system, coupled to an Analytik Jena PlasmaQuant Elite ICP-MS at UoP. The glass NIST 612 was used as primary standard and zircon reference materials 91500 (Wiedenbeck et al., 1995) and GJ-1 (Jackson et al., 2004; Piazolo et al., 2017) as secondaries. NIST 612 was analysed four times at the beginning and end of the session and twice per each group of unknowns. Every batch of analyses consisted of a combination of two NIST 612 bracketing four unknowns and two secondary standards. Laser operation conditions were 3 Hz, 3.5 J/cm^2. Laser spot sizes were 40 µm for NIST 612 and 30 µm for zircon. Each analysis consisted of 20 s of measured background and 30 s of acquisition. Twenty to 22 s were selected from the 30 s of acquisition, meaning that 4 or 5 s at the two extremities of the acquisition signal were excluded. Helium carrier gas flow was set to 0.3 L/min and plasma generation was set at 1300 W with

10 L/min of Ar plasma flow, auxiliary gas flow of 1.65 L/min and nebulizer flow of 0.9 L/min. The following masses were measured and had integration time of 10 ms: ^{29}Si, ^{49}Ti, ^{89}Y, ^{90}Zr, ^{139}La, ^{140}Ce, ^{141}Pr, ^{146}Nd, ^{147}Sm, ^{153}Eu, ^{157}Gd, ^{159}Tb, ^{163}Dy, ^{165}Ho, ^{166}Er, ^{169}Tm, ^{172}Yb, ^{175}Lu, ^{178}Hf, ^{232}Th, ^{238}U. Preferentially, analyses were located on top of the previous U-Pb and partially overlapping the previous Lu-Hf analyses (not more than 10-20% overlap). The raw data were reduced and corrected for instrumental drift using the Iolite 3.62 software (Paton et al., 2011). Zirconium content was used for internal calibration and measured via semi-quantitative analyses by Energy Dispersive X-ray Spectroscopy (EDS). A ZEISS Scanning Electron Microscope (SEM) with a silicon drift Oxford X-max 80 mm^2 detector (EDS) was used with a working distance of 14.8889 to 14.5011; EHT voltage of 20 kV and beam current of 500 pA. The in-house reference zircon ZRL-3 obtained from the Edinburgh Electron Probe facility was used for internal normalization and measured interspersed with unknown grains, yielding elemental concentrations within 5% accuracy. Oxide stoichiometry was therefore avoided and the zirconium content of the unknowns vary from 43 to 51%. No further corrections were applied. NIST 610 and secondary zircon reference materials yielded results within 10 - 15% accuracy relative to the recommended published values.

Rutile analyses were carried out at UFOP using a New Wave Research UP-213 laser ablation system (NdYAG) combined with an Agilent 7700x quadrupole ICP-MS. Rutile grains were ablated using spot sizes of 30 µm in diameter at a repetition rate of 10 Hz and laser fluence of 6-8 J/cm^2. Analyses were calibrated against R10 rutile (Luvizotto et al., 2009a) standard and data collected for 40 s after measurement of gas blank for 30 s. Oxide production was monitored as UO^+/U^+ and kept below 0.4%. The raw data were reduced using the matlab-based software package SILLS (Guillong et al., 2008). The measurements included the following isotopes: ^{27}Al, ^{29}Si, ^{49}Ti, ^{51}V, ^{52}Cr, ^{55}Mn, ^{56}Fe, ^{60}Ni, ^{66}Zn, ^{90}Zr, ^{93}Nb, ^{181}Ta, ^{182}W, ^{232}Th, ^{238}U. A total of 25 analyses were carried out in 21 rutile grains and Ti was used as internal standard for the grains assuming TiO_2 = 98%. Additionally, analyses of NIST 610 and NIST 612 were carried out with trace elements within 10% of published values with the exception of Nb (11%) and Ta (15%) for NIST 610; and Zn (15%) and W (15%) for NIST 612.

Results

U-Pb ages

Table 1 contains the summary of U-Pb analyses of this study. Zircon U-Pb analyses from the schist (sample B1a) are omitted in this table due to the different nature and age range of the grains. Detailed description of all zircon grains analysed and the results are presented below.

Samples from locality A

Zircon grains from the igneous samples are mostly prismatic and elongated. CL images reveal mostly dark domains throughout the grains, due to high U concentrations. Some grains show light cores, surrounded by dark rims. Some zircon grains show a bright structureless overgrowth surrounding weakly oscillatory-zoned dark cores. Metamict domains are pervasive and defined by corroded edges inside the grains (Fig. 4a). However, there are many concordant analyses. Fifteen zircon crystals from sample A1 yielded a Concordia age of 2949 ± 6 Ma, while 7 other zircon crystals returned another Concordia age of 3121 ± 7 Ma (Fig. 4a). Average Th/U ratios for both group of grains is ~0.2. A similar pattern was observed for zircon crystals from sample A2, which produce a Concordia age of 2827 ± 7 Ma (n = 8) with an average Th/U ratio of 0.12, and an upper Concordia intercept age of 3201 ± 6 Ma (n = 14) with Th/U average of 0.4 (Fig. 4b). Zircon age distribution spectra for these two Archaean intrusions are clearly bimodal (Fig. 4a; b). The relationship between the different domains as observed in CL images and their respective ages is not clear. Clear core-rim texture analyses do not show analytical differences, except for one analysis that is 23% discordant due to Pb loss. Overall however, the youngest ages obtained for the intrusions come from prismatic/elongated zircon crystals and are interpreted as crystallisation ages, whereas the oldest ages (c. 3200 Ma) mostly come from round zircon grains and are interpreted as inheritance assimilated during emplacement (Fig. 4a; b). The implications for such interpretations are discussed in the next section.

Samples from locality B

Zircon grains from the felsic intrusions of locality B are transparent, mostly euhedral, prismatic and have a typical magmatic oscillatory zoning in CL images, marked by dark and bright parallel stripes to the zircon regular crystal faces. Twenty-two zircon grains of sample B2a were dated by LA-SF-ICP-MS. Twenty analyses on concordant grains produced a weighted average $^{207}Pb/^{206}Pb$ age of 2143 ± 23 Ma and Th/U ratios average ~0.2. Ten of these zircon grains gave a Concordia age of 2127 ± 6 Ma, interpreted as the crystallisation age of this intrusion (Fig. 5a). One grain presents Archaean $^{207}Pb/^{206}Pb$ ages of 2936 ± 40 Ma (99.99% conc. - *Zr44core*) and 2718 ± 54 Ma (98.13% conc. - *Zr44rim*) (Fig. 5a). This grain has a contrasting morphology when compared to the majority of the zircon crystals dated from this sample (e.g. Fig. 5b), and it is interpreted as inherited from the country rock (presented below). Another twice-analysed zircon grain gave similar ages around 2130 Ma (*Zr14core; Zr14rim* - Fig. 5b).

Zircon grains from the host schist (B1a) are round and equant; they resemble 'soccer ball' zircon grains and show a complex growth history. A majority displays a dark core, surrounded by either a single bright rim or by multiple domains (Fig. 6). In the second case, CL images distinguish at least two zones: a medium grey zone that generally follows the dark cores and a lighter, almost white, finer rim. The transition between them often resembles a 'bleaching' effect (e.g. Schaltegger et al., 1999). This schist was sampled adjacent to a ~2130 Ma intrusion B2a; U-Pb analyses yielded only Archaean ages and Th/U ratios > 0.1 (Fig. 7a). Most were analysed in both cores and rims. Fifteen analyses are more than 2% discordant and were not plotted (though they are presented in the supplementary file). Seventy-four analyses are more than 99% concordant and produced ages ranging from 2670 ± 24 Ma to 3044 ± 18 Ma. The cores give $^{207}Pb/^{206}Pb$ ages ranging from 2690 ± 17 Ma to 3034 ± 18 Ma and Th/U ratios averaging 0.19, whereas the rims range in age from 2670 ± 24 to 3044 ± 19 Ma with Th/U ratios averaging 0.18. Although having the same overall range, core and rim age distributions are distinct (Fig. 7a): a probability density plot of concordant zircon grains shows that the main peak of age for the cores is at around 2940 Ma, whereas the main peak

of rim ages is c. 2690 Ma. Subordinate peaks reveal that the younger the cores, the smaller the peaks; and the younger the rims the higher the peaks. This pattern could be interpreted as a result of high temperature annealing, from inherited zones toward relatively younger rims (see discussions below) (e.g. Wan et al., 2011), smearing data along Concordia. In 29 analyses of rims and zircon grains with fir-tree zoning, acquired at UoP, the $^{207}Pb/^{206}Pb$ ages vary from 2699 ± 45 to 2935 ± 39 Ma and form a similar spectrum to the rims analyses acquired at UFOP (Fig.7a). Th/U ratios are variable, ranging from 0.05 to 0.7 with an average of 0.13. The two youngest $^{207}Pb/^{206}Pb$ ages, 2699 ± 45 and 2688 ± 56 Ma, have Th/U ratios of 0.20 and 0.17, respectively. The morphology of cores and age distribution of soccer ball zircon grains support a detrital origin for the older cores with annealing-related high temperature conditions smearing ages along Concordia because of a potentially prolonged peak of metamorphism at 2680 Ma (e.g. Whitehouse and Kemp, 2010). Additional evidence for this interpretation is presented in the discussion section and is reinforced both by Hf isotopes in the same zircon grains and trace element analysis in zircon and rutile (presented below). Alternative interpretations are also discussed.

Rutile grains analysed by LA-ICP-MS are euhedral to subhedral, range in size from 30 to 500 µm. Most grains are >90% concordant, with 4 grains being concordant. Measured but not common Pb corrected $^{207}Pb/^{206}Pb$ ages vary from 2118 ± 42 Ma to 2596 ± 30 Ma. Archaean and Palaeoproterozoic grains are indistinguishable both petrographically and in BSE imaging. Acicular ilmenite inclusions are common, but inclusion-free areas could easily be targeted for U-Pb and trace element analysis. The grains have low common Pb, and with very low Th contents, the ^{208}Pb-based common Pb correction was preferred, avoiding Hg interferences. Following common Pb correction, two grains have $^{207}Pb/^{206}Pb$ ages of 2570 ± 110 Ma and 2632 ± 46 Ma (96-97% concordant), with the remaining grains having ages between 2060 ± 109 Ma (88 % concordant) and 2338 ± 108 Ma (97% concordant) (see supplementary material). Ignoring the grains with Archaean memory, twelve with low common Pb contents produce an upper intercept age of 2173 ± 27 (MSWD = 1). The same group of analyses, after common Pb correction and error propagation comprise an intercept age at 2149 ± 26 Ma

(MSWD = 1.08). Thirteen grains with less than 0.2% $^{206}Pb_c$ yield an intercept age of 2172 ± 33 Ma and are considered the best age of 'reset' rutile grains, this being a good estimate of the age of that thermal resetting event (Fig. 7b). This ~2140 Ga event recorded in the rutile grains is considered to be the same event observed in the felsic intrusions adjacent to the schist and appears to have had no effect on zircon grains within schist sample B1a.

Forty-six U-Pb analyses were performed out on 39 zircons from sample B2b, all >96% concordant. Eight gave $^{207}Pb/^{206}Pb$ ages of 2912 ± 21 Ma to 2778 ± 19 Ma with an average Th/U of 0.12, whereas the other 31 yielded Palaeoproterozoic ages varying from 2183 ± 29 to 2087 ± 30 Ma and Th/U ratios averaging 0.14. The younger group gives an upper intercept age of 2135 ± 16 Ma (MSWD = 3.3) (Fig. 8a). One of the largest zircons (575 µm) had multiple analyses that span a duration of ~30 Myr, but if considered together, a weighted mean average of all 5 analyses gives 2125 ± 16 Ma (Fig. 8b). Two round zircons with cores and rims produced ages of 2912 ± 22 Ma and 2778 ± 19 Ma, and 2831 ± 18 Ma and 2890 ± 21 Ma, respectively for cores and rims. These Archaean ages are interpreted as inherited from host rocks, whereas the 2135 ± 16 Ma is considered as the crystallisation age of the intrusion.

Twenty-seven out of 50 U-Pb zircon concordant to near (>97%) concordant analyses from sample B2c, give an upper intercept $^{207}Pb/^{206}Pb$ age of 2133 ± 28 Ma (MSWD = 2.3) and are interpreted as the crystallization age of the sample (Fig. 9). The remaining 23 zircon analyses gave a range of Archaean ages from 3177 ± 17 Ma to 2697 ± 19 Ma, with most zircon ages at c. 2860 Ma (Fig 9); Th/U ratios average 0.38. Similarly to sample B2a, Archaean ages were obtained from round zircons and are interpreted as inherited. Palaeoproterozoic ages are from slender euhedral zircons and are interpreted as the crystallisation age of the intrusion.

Sample from locality C

Zircons from this sample are prismatic and euhedral and show typical magmatic oscillatory zoning, similar to the elongated zircons commonly present in the felsic intrusions from locality B. Aside from two concordant inherited Archaean grains ($^{207}Pb/^{206}Pb$ age of 2688

± 17 Ma and 3363 ± 17 Ma), 13 concordant to subconcordant zircons have Palaeoproterozoic ages, out of which the 7 most concordant analyses (>99%) define an intercept age of 2130 ± 30 Ma (MSWD = 0.21). Their average Th/U ratio was 0.31 and this age is interpreted as the crystallisation age of the intrustion (Fig. 10).

Lu-Hf isotope analysis

Combined Lu-Hf and U-Pb analyses in zircon can distinguish juvenile from recycled magmas. Juvenile magmas are essentially mantle-derived and are characterized by positive initial εHf, whereas recycled magmas are defined from remelting of older crust and negative εHf (Vervoort and Kemp, 2016 and references therein). Although recently debated (Payne et al., 2016), Hf isotopes can be used to calculate a model age value (T_{DM}) representing the maximum age of magma extraction from the depleted mantle. Therefore, considering the U-Pb age previously obtained in a zircon crystal, the initial Hf composition of such zircon represents the $^{176}Hf/^{177}Hf$ value at the time of its crystallisation. The model age is also described as the crustal residence time for the rocks where the zircons were extracted. In this paper, we treat model ages as recommended by Vervoort and Kemp (2016), which means in a qualitative and general sense.

Sixty zircons from sample B1a and 22 zircons from sample B2a were selected for Hf isotope analysis. The analysed grains are concordant or sub-concordant and had plenty of material left after the U-Pb analyses. Among the sampled intrusions, B2a is the freshest and offered the most translucent zircons, being therefore the best candidate for such analyses.

Except for three inherited Archaean grains (2715 ± 39 Ma, 2718 ± 54 Ma and 2936 ± 40 Ma), all chosen zircons from sample B2a are Rhyacian, ranging in $^{207}Pb/^{206}Pb$ age from 2122 ± 42 to 2177 ± 40 Ma. This younger group of zircons has an average $^{177}Hf/^{176}Hf_{(t)}$ = 0.281188 ± 0.000018, which yields $\varepsilon Hf_{(t)}$ values around -8, whilst the oldest two grains (2172 ± 47 Ma and 2177 ± 40 Ma) of this group have values of -3.2 and -6.4, respectively (Fig. 11). Only one Rhyacian zircon yielded positive $\varepsilon Hf_{(t)}$ value of +1.3 in its core and together with one Mesoarchaean grain (2936 ± 40 Ma), which provided the $\varepsilon Hf_{(t)}$ value of +2.1, are the only two

grains possessing a mantle-derived signature among all the analysed zircons of sample B2a. The two Neoarchaean ages, 2715 ± 39 Ma and 2718 ± 54 Ma, provided $\varepsilon Hf_{(t)}$ values of -3.3 and -2.2, respectively. The model ages of the zircons lay in an interval between 3.2 and 3.6 Ga. The Rhyacian mantle-derived grain ($\varepsilon Hf_{(t)}$ = +1.3) has a T_{DM} of 2.42 Ga and is 2126 ± 37 Ma old. Notably, this same zircon produced a crustal-derived signature for its rim ($\varepsilon Hf_{(t)}$ = -9.9), although with identical $^{207}Pb/^{206}Pb$ age of its core component (2130 ± 38 Ma) (Fig. 5b).

Zircons from sample B1a show a large range of Hf composisiton, with Hf values from -7.9 to +5.5 ($^{Hf}T_{DM}$ ages interval: 2.9 – 3.6 Ga), respectively to ages varying from 2680 ± 60 Ma to 3044 ± 38 Ma. This dispersion of $\varepsilon Hf_{(t)}$ nonetheless increases through time, becoming more negative the younger the ages, either for cores or rims (Fig. 11b). Palaeo- and Mesoarchaean zircons show a spread in $\varepsilon Hf_{(t)}$ from -3 and +5 and Neoarchaean zircons have $\varepsilon Hf_{(t)}$ values consistently more negative (+4 to -8). All rim analyses younger than 2780 Ma did not yield any positive $\varepsilon Hf_{(t)}$ value (Fig. 11b).

Trace element geochemistry

Sixty-one trace element analyses were carried out on 51 grains from sample B1a. A few analyses were excluded due to the presence of peaks in the ^{49}Ti isotope during acquisition. Although not visible in BSE and/or CL images, these peaks potentially indicate inclusions or fractures (e.g. Fu et al., 2008). Thirteen analyses were located adjacent/partially overlapping spots that were selected for U-Pb-Hf isotopic analysis; and twelve on spots previously analysed only for U-Pb geochronology. The remaining 36 analyses were carried out on zircon grains with only textural zonation control (CL and BSE imaging). No or slightly negative europium anomalies are recorded in most of the grains and they can be distinguished in two groups (Fig. 12). The first group (light grey) has a general positive slope of mid to heavy REE with variable concentration (100 – 1000 times the chondritic value) and positive or absent Ce anomaly. On average, the $Eu/Eu_{(N)}$ is 0.47 (varying from 0.27 to 0.65) and the $Lu/Gd_{(N)}$ is 34 (varying from 4.2 to 95), due to a variable degree of fractionation. The second group (black)

is characterized by a flat heavy REE pattern compared to the first group, and its compositional variation is restricted. For example, the $Eu/Eu_{(N)}$ for the black REE patterns (Fig. 12) varies from 0.39 to 0.52 (average of 0.46) and the $Lu/Gd_{(N)}$ varies from 0.16 to 0.66 (average of 0.24). These two groups are also distinguished by their absolute concentrations of the heavy REE, the second one (black) being relatively more enriched than the first (grey). The titanium concentrations of these zircons are variable in first group (12 to 36 ppm), but restricted in the second (20 to 25 ppm).

Twenty five analyses were carried out on rutile grains from sample B1a and 21 of them were located adjacent to the U-Pb spots. Analyses show variable Zr content ranging from 320 to 5603 ppm (average 850 ppm), give temperature of 735°C (Ferry and Watson, 2007), 847°C (Zack et al., 2004) and 741 °C (Tomkins et al., 2007 – assuming pressure of 10 Kbar) (Fig. 7b). Niobium concentrations average ~15000 ppm and vary between 4362 and 24944 ppm. Chromium concentrations are low with most of values below 100 ppm. Vanadium concentrations average 460 ppm and vary from 222 to 647 ppm. The presence of abundant Ilmenite inclusions were identified by the ^{56}Fe peak in the analyses, which when encountered were then discarded.

Discussion

Timing of greenstone belt formation in the SSFC

Geochronological data from the Rio das Velhas Supergroup are still scarce. Volcanoclastic graywackes from the upper part of the sequence dated by Noce et al. (2005) yielded ages of 2792 ± 11, 2773 ± 7 and 2751 ± 9 Ma and represent three volcanic events intercalated by clastic sediments. Hartmann et al. (2006), based on SIMS geochronology of detrital zircons from two sandstone samples, established a maximum depositional age for the Nova Lima Group of 2749 Ma. Moreira et al. (2016), in a study involving analyses of more than a thousand zircon grains, determined a maximum depositional age for the Maquiné Group of 2730 Ma. The ages between 2800 Ma and 2760 Ma correspond to the Rio das Velhas II of

Lana et al. (2013), whereas the ages between 2760 and 2680 Ma correspond to the Mamona event of Farina et al. (2015). The present published ages give only a maximum age for the greenstone belt of the QF and there is no well-defined study bracketing the greenstone belt age in the SSFC, particularly its lower portion. In other words, the lower part of the group has no constraints and the Meso- to Neoarchaean origin of the sequence is as yet an assumption (Lana et al., 2013; Van Acken et al., 2016; Fonseca et al., 2017; Verma et al., 2017).

Our newly obtained crystallisation age 2948 ± 3 Ma for one of the granitoid intrusions (sample A1) provides a minimum age for the Rio das Velhas greenstone belt in the SSFC. Considering the prismatic and elongated habit and the presence of magmatic oscillatory zoning in the CL images of the youngest grains (Fig. 4a), the crystallisation age of the intrusion can be reasonably defined at 2948 ± 3 Ma. We consider it unlikely that this age represents inheritance, since this would imply both an absence of igneous zircons and no morphological alteration of prismatic slender inherited grains by a hypothetical younger melting event. This implies that the greenstone belt spans more than 200 Myr and supports the hypothesis of greenstone belt thrusting concomitant with island arc accretion in the early phases of the RVI event (Lana et al., 2013). The older ages obtained for this sample, here interpreted as inherited, are distributed in the interval between 3224 Ma and 3096 Ma and suggest recycling of Palaeoarchaean crust, a fragment of which, dated at 3220 - 3200 Ma, is preserved in the eastern part of the QF (Lana et al., 2013). A similar set of ages has been documented in the Santa Rita Dome where a coarse-grained massive trondhjemite yielded zircons with inherited cores dated at 3219 ± 13 Ma and overgrowths significantly younger at 2898 ± 7 Ma, interpreted as the crystallisation age (Lana et al., 2013).

Another intrusion from the same sampling site (sample A2) yielded an age of 2827 ± 3 Ma. This age does not correspond to any known period of magmatic activity in the region. However, similar ages have been recorded, although very rarely, in the age distribution pattern of some detrital zircons of the Minas Supergroup (*cf.* Mendes et al. 2014; Martinez Dopico et al., 2017), possibly indicating the occurrence of a small and isolated igneous pulse around

2820 Ma. Sample A2 also records numerous inherited Palaeoarchaean ages in the 3218 - 3166 Ma interval. The older group of zircons, i.e. ages around 3200 Ma, are inherited grains either from the source or by assimilation during intrusion. Both younger ages (2948 ± 3 Ma and 2827 ± 3 Ma) are interpreted as crystallisation ages. In this sense, considering the nature and spatial distribution of the samples (see details in samples description) it is reasonable to suggest that the event(s) which led to the generation of these intrusive bodies at upper crustal levels lasted at least 110 Ma, and their source supports the hypothesis of the Santa Bárbara Palaeoarchaean crust as the precursor for the evolution of the SSFC defined by Lana et al. (2013) and supported by many detrital zircon studies (e.g. Hartmann et al., 2006; Koglin et al., 2014; Moreira et al., 2016; Martinez Dopico et al., 2017). Such inherited zircons also confirm the hypothesis of reworked crust in the SSFC during the Palaeoarchaean, where a regime ruled by TTG production and crustal growth, gave place to a regime dominated by reworking processes in the Neoarchean (Albert et al., 2016).

Archaean metamorphic facies

Zircons from sample B1a and the inherited Archaean zircons from sample B2a have very striking morphological features. Their round to ovoid and often multifaceted (‘soccer ball’) external shape, their transparency and predominantly pale-pink colour, as well as their complex internal structures showing common sector and fir-tree zoning, contrast strongly with all other zircon samples described in the QF (e.g., Hartmann et al., 2006; Noce et al., 2005; Lana et al., 2013; Farina et al., 2015; Moreira et al., 2016; Martinez Dopico et al., 2017 and many others). The occurrence of a homogeneous and abundant population of zircons with such characteristics in apparently relatively low grade Archaean greenstone belt rocks (epidote-chlorite-quartz-schist or white mica-chlorite-quartz-schist) is unexpected.

Detailed observation of the CL images show very clearly that grain roundness could not be the product of sedimentary abrasion, but that the grains were overgrown and acquired their shape during a high-grade metamorphic event (Fig. 6). The complexity of these structures

also excludes a direct magmatic origin for this population because the preserved features have been widely described as common to metamorphic zircons formed in high-grade conditions, more specifically in granulite (e.g. Vavra et al., 1996) or eclogite (e.g. Rubato et al., 1999) facies. The same occurrence of equant grains are rarer but also present in medium to high amphibolite facies (Rubatto, 2017). U-Pb and Lu-Hf analyses show that the majority of the grains have two rims around preserved truncated magmatic cores, although grains with multiple metamorphic overgrowths are present and are suggestive of multiple reactions periods of growth (Fig. 6). In general, the younger rims have lower $\varepsilon Hf_{(t)}$ signature and rims with positive $\varepsilon Hf_{(t)}$ values are older than 2770 Ma (Fig. 11b). Regarding the theoretical model for the growth processes leading to the formation of soccer ball-shaped zircons, the most accepted hypothesis involves the so-called roughening transition (Vavra et al., 1996) and recrystallisation of the cores followed by annealing of the rims (Schaltegger et al., 1999). This is because equant morphologies are favored over developed prisms when they grow in a solid state in a solid matrix. Given that domains in a zircon often truncate the oscillatory zoning pattern of the domain they are surrounding (Fig. 6), it is reasonable that dissolution preceded new growth, with multiple phases of dissolution and growth possible (e.g. Vavra et al., 1996; Corfu et al., 2003; Korhonen et al., 2014; Taylor et al., 2016).

The inherited cores with magmatic oscillatory zoning are present but rare and, in general, they are sharply truncated by the overgrowths. These cores might have undergone a certain degree of recrystallisation during the metamorphic events as extinguished growth banding is characteristic of most of the dark cores. Nonetheless, the U-Pb analyses in these domains suggest a Mesoarchaean age of the protolith (Fig. 7a). The beginning of the metamorphism is marked by a grey luminescence that truncates the partially recrystallised cores. The seams between the cores and the first generation of rims suggests a process of rounding by resorption. The most remarkable features of these domains are the bleached zones that causes a variance of brighter luminescence towards the outer edges. However, the similar textures seem to have formed at dissimilar times as a large spread of ages on the

Concordia line is observed for both cores and rims (Fig. 7a) and genuine overgrowths can be distinguished from bright Pb loss zones (Fig. 6 – grain Zr74). The spread of metamorphic ages nevertheless points towards c. 2700 - 2680 Ma and was likely caused by multiple processes in different inherited zircons during a high temperature metamorphic process (Taylor et al., 2016). Low values (<0.1) for Th/U are a small contribution in the overall signature observed in zircons from sample B1a, as most of the grains have Th/U > 0.2. High-grade metamorphic zircons such as those from granulite and eclogite-facies are usually relatively high in Th/U ratios (Santosh et al., 2009; Wan et al., 2009; Grant et al., 2009), although different ratios have been reported elsewhere, as the ratio is primarily controlled by the metamorphic assemblage of the rock (Harley et al., 2007; Rubatto, 2017). Recrystallization/regrowth of zircon under these conditions is marked by the absence of co-existing high-Th phases (such as monazite, epidote and allanite), which make zircons incorporate preferentially Th over U (e.g. Yakymchuk et al., 2018). Another reason may be that high-grade metamorphism forces fluids out of the rock system, thus removing U which is more fluid-mobile than Th.

Ti-in-zircon and metamorphic petrogenesis

Zircons yielded Ti contents in the range of 12 to 36 ppm. Three analyses with respectively 60, 95 and 123 ppm of Ti were not considered in this study. The presence of micro-inclusions of a Ti-rich phase could be possible explanations for the high Ti contents obtained and justify the exclusion of such values (e.g. Ewing et al., 2013). The abundant quartz and rutile throughout the sample suggest the coexistence of these minerals during the initial metamorphic conditions. Thus, for the Ferry and Watson (2007) thermometer, $a\mathrm{SiO_2}$ and $a\mathrm{TiO_2}$ are assumed to be 1.0. A lower $a\mathrm{TiO_2}$ (i.e. 0.7) would increase the temperature output, whereas a lower $a\mathrm{SiO_2}$ would decrease it. In this case, we consider unlikely the estimated temperature to be lower than the values yielded when the chosen activity is 1.0, mostly because quartz is abundant in the sample.

The Ti-in-zircon thermometer yielded temperatures between 740 and 890 °C and indicate that restricted high temperature domains are generally younger, highlighted in black in Fig. 12b. Conservatively, the upper quartile of the temperatures defines the peak at 823 °C (Clark et al., 2019), which corresponds to the temperatures of the zircon grains with Ti concentrations between 20 and 24 ppm (Fig. 12a). The same group of analyses have low $Lu/Gd_{(N)}$ (< 0.7) and small to absent Eu anomalies, indicating growth in the presence of eclogitic minerals and absence of plagioclase. The enrichment of MREE compared to the other groups suggests that monazite and titanite were not concurrent phases during zircon growth (Peucat, et al., 1995; Kohn, 2017). The second group of zircons display a broader range of crystallization temperatures, but they are devoid of evidence for coexistent garnet growth (Rubatto, 2002; Rubatto and Hermann, 2007a). This group has an average $Lu/Gd_{(N)}$ of 34 and shows a large range of HREE values spanning two orders of magnitude (Fig. 12a). The trace element compositions show no systematic pattern with $^{207}Pb/^{206}Pb$ ages (Fig. 12b). As the groups partially overlap in age, it suggests a system controlled locally by incipient sub-solidus growth of garnet (Taylor et al., 2017), in which there is no efficient trace element mobility, and where small-scale equilibrium between zircon and garnet happened over short distances. On the other hand, the variance of HREE pattern in the rims could be explained by the continuous loss or break-drown of garnet, making the elements available for zircon intake. This indicates that the zircons which yield more radiogenic $^{176}Hf/^{177}Hf$ values could have grown within a small-volume melt, trespassing the sub-solidus metamorphic recrystallisation limit (Taylor et al., 2015). Sector and fir-tree zoning also argue for the presence of anatectic melt during high-grade metamorphism (e.g. Kelly and Harley, 2005; Kunz et al., 2018). However, the authors are inclined to the sub-solidus explanation in absence of metamorphic fluids. The hypothesis is reasonable given the absence of Eu anomaly, the relative enrichment of MREE in the black curves pattern, the overall Th/U > 0.1 and the variable HREE concentrations for the light grey curves, which all indicate a monazite-feldspar-free paragenesis (Peucat, et al., 1995; Rubatto and Hermann, 2007b, Yakymchuk et al., 2018). Regardless, the involvement of a possible small volume of unconnected pockets of melt, the scatter of both ages and zircon trace

element compositions point to local-scale equilibrium controlled by garnet and recrystallisation.

Zr-in-rutile, traces and metamorphic petrogenesis

Zr concentration in the rutile grains varies by more than one order of magnitude from 320 to 5603 ppm and temperatures based on Zr-in-rutile thermometry average 735 °C (Ferry and Watson, 2007), 847 °C (Zack et al., 2004), and 741 °C (Tomkins et al., 2007). These temperatures are incompatible with the current (retrogressed) greenschist facies assemblage of the rock. One possible explanation is that the Ti-rich phase records the highest temperature undergone by the rock during its history, with only the U-Pb system being disturbed (e.g. Korhonen et al., 2014). Experimental diffusivity studies in rutile (e.g. Cherniak, 2000; Cherniak et al., 2007) show that Pb diffuses much faster than Zr, by one to almost two orders of magnitude. Therefore, Zr content in rutile is commonly decoupled from the U-Pb dating performed in the same grain and might provide information on the older history of the rock (Zack and Kooijman, 2017). This hypothesis is plausible as it also matches with the Ti-in-zircon temperatures from the same rock, which records the lowest temperature at 735 °C. Therefore, the high temperatures obtained appear realistic, considering the high-grade metamorphic nature of the Archaean protolith, consistent with zircon morphology and U-Pb age distribution. Thus, the temperature given by the Zr-in rutile thermometry records high pressure granulite facies stages of the metamorphic rock at depth and growth of both zircon and rutile. Subsequently, metamorphic overprint is recorded by the rutile age reset during the collisional process at c. 2130 Ma.

Rutile grains show recrystallization textures after dissolution of ilmenite (supplementary material). Experiments of Ca-rich compositions show similar textural relationship of unstable ilmenite replaced by subhedral rutile (titanite absent) at conditions above 1.3 GPa and 550 °C (Angiboust and Harlov, 2017). As a caveat, these experiments were realized at low oxygen fugacity and the infiltration of high-fO_2 fluids during metamorphism could significantly reduce the absolute pressure value (Guo et al., 2017). Nevertheless, these

are likely the conditions at which the c. 2130 Ma reaction took place: at relatively high pressures but low temperatures. As ilmenite and rutile still coexist and Zr was not re-equilibrated, the temperature for the amphibolite facies reaction can be estimated at ~ 480°C (Luvizotto et al., 2009b). Thus, the ilmenite inclusions present in the rutile grains are relict, later crystallised to rutile as suggested by Angiboust and Harlov (2017) under prograde metamorphism (Luvizotto et al., 2009b).

The exceptionally high Nb (average of 15000 ppm) and low Cr (>100 ppm) contents are characteristic of felsic granulite-facies rocks and similar occurrences of detrital rutiles with even higher concentrations are reported elsewhere (e.g. Meinhold et al., 2008). We interpret the high Nb/Cr ratios as evidence for a detrital source, given the apparent sedimentary nature of the protolith (Zack et al., 2002). Regardless of their age, rutile grains have similar trace element concentrations. The presence of Archaean rutile with similar signature to the Palaeoproterozoic grains suggests that although reset in terms of U-Pb age, the trace element composition represents the original crystallization of rutile in the Archaean (Fig. 7b).

Archaean metamorphism events in sample B1a

Overall, the occurrence of older zircon cores to younger rims, associated with a general decreasing of $\varepsilon Hf_{(t)}$ values (Fig. 11b) and the morphological features of the soccer ball zircon grains favours the hypothesis of high-grade metamorphism of the protolith of sample B1a under 'dry' conditions, zircon recrystallisation and rutile growth. This cryptic event belies the greenschist metamorphic assemblage and complete lack of high grade minerals in the rock at the present time. The large overlap of the zircon ages scattering along the Concordia line (Fig. 7a) demonstrates the re-adjustment of the U-Pb system to various degrees, culminating in the almost continuous distribution of the rim ages from 2780 Ma to 2680 Ma. This spread over a long time span cannot be the product of a continuous period of zircon formation, neither in an igneous nor in a metamorphic context. This age distribution pattern is thus most likely the result of 'age dispersion' due to partial resetting of the U-Pb isotopic system during zircon recrystallisation (e.g. Kröner et al., 2014; Taylor et al., 2016). In this sense, the genuine

overgrowths are represented by the youngest dated rims, whereas rims that are relatively older are in fact high temperature Pb loss. The older ages are nevertheless not meaningless, since they testify to Mesoarchaean contributions, strongly suggesting an inheritance origin for the protolith zircon grains under different degrees of age mixing efficacy and localized garnet growth. Most of the rutile grains have reset U-Pb systematics at c. 2130 Ma and only a few Archaean grains were preserved (Fig. 7b). They are slightly younger than the zircon metamorphic peak and could represent cooling during the Archaean retrograde path. On the other hand, they could represent an even older detrital source, partially affected by the Palaeoproterozoic resetting. Although the answer is not tangible with the current dataset, the presence of Archaean rutile grains in this rock is unambiguous.

The metamorphic ages match peaks from igneous and detrital zircon grains from potassic granitoids, which were emplaced during the Mamona event (2760 - 2680 Ma). The high-K granites generated in this period of magmatic activity are distinguished from the TTG-like rocks produced in the preceding events recorded in the QF. An origin through partial melting of metasedimentary rocks was invoked by Farina et al. (2015) to explain the contrasting chemical features of the granites produced during this period and later confirmed by O isotope analyses in zircon grains (Albert et al., 2016). According to these authors, the chemical and mineralogical characteristics of the high-K granites suggest that they were produced by low degree partial melting of metagreywackes. The generation of high-K granites and that of sample B1a zircon grains have the same ages and are ascribed to similar processes. The question whether the schist, in its earlier high-grade form, could be a possible melt source involved in the generation of these granites cannot be answered. It is nevertheless reasonable to assume that they were both generated in the same geological context and the Mesoarchaean detrital zircon grains were metamorphosed in situ at c. 2680 Ma.

The discovery of a zircon population representing evidence of high-grade metamorphic conditions involving supracrustal rocks supports a crustal thicknening model, in a context of an overall high thermal gradient. Evidence for similar metamorphic conditions are reported in the Passa Tempo metamorphic complex to the west of the QF, which reaches granulite facies

under crustal reworking and collisional tectonics between 2.72 and 2.55 Ga (Teixeira et al., 2017 and references therein). Globally, these conditions are broadly recorded at c. 2.8 Ga (Brown and Johnson, 2018) and conceived to represent shallow subduction and thickening of the crust (Foley et al., 2003; Pearson et al., 1995). It also could represent an important timekeeper of the onset of subduction and crustal thickening related to greenstone belt basin closure in the late Archaean.

Timing of tectonic collision in the Palaeoproterozoic

The age of the Palaeoproterozoic intrusions in the Itatiaia block can be reasonably defined at 2130 Ma, considering the average age of the analyses and the Concordia ages given by samples C1, B2a, B2b and B2c (Fig. 5, 8, 9, 10; Table 1). This set of intrusive bodies is temporally correlated with the main peak of magmatism of the Alto Maranhão Suite (Seixas et al., 2013; Moreira et al., 2018), defined as a large juvenile magmatism that borders the SSFC margin and comagmatic suites (e.g. Ávila et al., 2010; Teixeira et al., 2015 and references therein). Despite the well-described compilation of geographic position and main suites in the MB (e.g. Barbosa et al., 2015), the understanding of the reaction of the Palaeoarchean crust during the amalgamation of the Palaeoproterozoic orogeny remains poorly constrained. It is clear that the MB was not built upon the continental margin but rather collided/docked with the cratonic margins. However, it is still not clear how far the craton was heated and deformed during the thermal peak of the magmatic accretion in the Palaeoproterozoic (Aguilar et al., 2017). In this context, the intrusions fit the tectonic stage of uplift and progressive deformation of the Palaeoproterozoic foreland as the orogen developed. They could either represent the magmatism that penetrated the foreland of the orogen or be local melts produced during the metamorphism that coincides with the stacking of thrust layers. Either interpretation can be used to better understand the collisional period, as a window to rocks at depth or local anatexis of the upper crust.

Owing to the fact that most of the 2130 Ma zircon grains analysed in this study have a crustal signature ($\varepsilon Hf_{(t)} \approx$ - 7 to -10) and only one has a mantle source origin ($\varepsilon Hf_{(t)}$ = +1.3)

(Figure 11b), one can suggest that the magmatic penetration into the continental crust describes how the craton behaved during the docking of the MB. As the intrusions, C1, B2a, B2b and B2c, belong to the peak of the Rhyacian orogen, a mechanism to explain the difference of the crustal-derived signature is necessary, since the MB defines almost an exclusive juvenile segment (Seixas et al., 2013; Teixeira et al., 2015; Moreira et al., 2018). The difference of ~11 Hf epsilon units could for example be explained by infracrustal reworking during collision. In this case, the contamination could have happened via the same mechanism, which formed the crustal-derived segments with low $\varepsilon Hf_{(t)}$ in the MB (Barbosa et al., 2015): magmas were contaminated by mixing with pre-existent crust of the MB or older crustal-derived segments at the Archaean margins. This hypothesis is nevertheless less probable, because the scale and characteristics of these minor intrusions are more compatible with partial melting of local metasedimentary rocks. Moreover, at this stage, a dehydrated crust underlies the thick Rio das Velhas and Minas Supergroup sedimentary sequences (Romano et al., 2013), and perhaps across the region, preventing subsequent remelting at depth or penetration of Palaeoproterozoic magmas. Among other effects, this explains the small volume of Rhyacian magmatism within the Archaean domains of the SSFC (Alkmim and Marshak, 1998), as Palaeoproterozoic melts require melt-fertile rocks.

The event following orogenic collision consists of the exhumation of the Archaean block, acting as the substrate for the sedimentary sequence deposition. The development of the magmatic arc promoted the displacement of the segment towards the cratonic foreland (Aguilar et al., 2017). The brittle-ductile faults in the strata belong to the latest advancements of the deformational front. This system has been reactivated during the Brasiliano orogeny, thrusting the sedimentary sequences towards the west. This tectonic process also shuffled the stratigraphic order of the layers, giving the current observed geological contact. Thus, as the Rhyacian orogen was built up, the early basement was being exposed and acted as the substrate for the chrono-correlated foreland basin (i.e. the Sabará Group; Reis et al, 2002; Renger et al., 1995).

The data of this study provide evidence of Palaeproterozoic magmatism within the SSFC boundaries, and together with previous similar age occurrences (e.g. Carvalho et al., 2017) demonstrate how the Archaean nucleus was affected by the Palaeoproterozoic collisional magmatism. Therefore, Rhyacian zircon grains from the intrusions of this study describe: 1) a history of the Archaean basement as a hinterland (>2600 Ma); 2) the peak of magmatism and crustal thickening (2130 to 2100 Ma); 3) and partially the exhumation that predates the formation of the dome-and-keel structure in QF. In a broader perspective, these intrusions reveal new insights that were not apparent from the study at larger scale and so should be studied more extensively in other orogens to reveal subtle aspects of collisional processes. They also mirror the amalgamation of the Columbia/Nuna supercontinent in the context of global tectonics (e.g. Meert, 2012).

Conclusions

Zircon grains from felsic intrusions and rutile and zircon grains from host greenschists at the edges of the SSFC were analysed in order to constrain the Archaean and Palaeoproterozoic tectono-thermal amalgamation periods of the region. Our U-Pb-Hf isotope and trace element analyses reveal the following:

1) Crustal segments as old as 3200 Ma were present in the first events of the SSFC as testified by inherited zircon in the studied samples. This is also evident from the detrital zircon record of Archaean and Palaeoproterozoic metasedimentary sequences. The apparent absence of such ages in the basement complexes suggests an intense recycling/overprint regime;

2) A small felsic intrusion into the Rio das Velhas schists was dated at 2948 ± 3 Ma constraining the evolution of the greenstone belt from >2950 Ma to 2700 Ma, and confirming the Mesoarchaean timing for the formation of the ultramafic basal sequences of the QF;

3) High-grade metamorphic zircon grains preserved in a thoroughly retrogressed greenschist are consistent with the final stage of Archaean crust amalgamation, thickening and emplacement of granitoids resulting in the cratonic stabilization at c. 2690 Ma;

4) The Rhyacian docking involved the Archaean and Palaeoproterozoic supracrustal sequences (Rio das Velhas and Minas supergroups) and promoted a low degree of partial melting of sediments at upper crust level. This implies a dynamic tectonic evolution between the Minas accretionary orogeny and the SSFC, once the Archaean sequence also acted as a substrate for the Minas sequence deposition;

5) Prograde metamorphic reactions in the sequence are represented by detrital ilmenite reaction to rutile. Resetting of the U-Pb system at high pressure – low temperature conditions represents the collisional stage at c. 2130 Ma;

6) The Rhyacian intrusions mirror the magmatic activity of the Mineiro Belt during its accretionary stage. The lack of regional magmatism within the SSFC corroborates its role as the hinterland of such an episode, in which deep Archaean crust was refractory as the Palaeoproterozoic melts were formed.

Acknowledgements

Hugo Moreira acknowledges CNPq (National Council for Scientific and Technological Development) grant (234610/2014-0), Randall Parrish for enlightening geological discussions and Inês Pereira for insightful rutile petrochronology conversations. Cristiano Lana and Craig Storey acknowledge funding from CONFAP-The UK Academies – APQ-00688-16. We thank Ana R. Alkmim for performing the Lu-Hf analyses on zircon grains of this study and Fernando F. Alkmim for field work guidance. We also thank Catherine Mottram for critical comments on an early version of this manuscript. We acknowledge Rich Taylor and an anonymous reviewer for their detailed comments on this manuscript. We also wish to acknowledge funding from CNPq (401334/2012-0, 302058/2015-0, 402852/2012-5) and FAPEMIG (APQ-03793-16) grants and Edital UFOP Auxílio a pesquisador 2017. Lastly, we appreciate the efficient and careful editorial handling by Marco Scambelluri.

References

Aguilar Gil, C., Alkmim, F.F., Lana, C., Farina, F., 2017. Palaeoproterozoic assembly of the São Francisco craton, SE Brazil: New insights from U–Pb titanite and monazite dating. Precambrian Research 289, 95-115.

Albert, C. , Farina, F., Lana, C., Stevens, G., Storey, C., Gerdes, A., Martínez Dopico, C., 2016. Archean crustal evolution in the southern São Francisco craton, Brazil: constraints from U-Pb, Lu-Hf and O isotope analyses. Lithos 266-267, 64-86.

Alkmim, F. F., Marshak, S., 1998. Transamazonian Orogeny in the Southern São Francisco Craton Region, Minas Gerais, Brazil: evidence for Paleoproterozoic collision and collapse in the Quadrelátero Ferrífero. Precambrian Research, 90, 29 – 58.

Alkmim, F.F., Martins-Neto, M. A., 2012. Proterozoic first-order sedimentary sequences of the São Francisco craton, eastern Brazil. Marine and Petroleum Geology. 33, 127–139. doi:10.1016/j.marpetgeo.2011.08.011

Alkmim, F.F., Teixeira, W., 2017. The Paleoproterozoic Mineiro belt and the Quadrilátero Ferrífero. In: Heilbron, M., Alkmim, F., Cordani, U.G. (Eds.), The São Francisco Craton and its margins, Eastern Brazil, Geology Review Series. Springer-Verlag. 71–94. http://dx.doi.org/10.1007/978-3-319-01715-0_5. Chapter 5.

Angiboust, S., Harlov, D., 2017. Ilmenite breakdown and rutile-titanite stability in metagranitoids: Natural observations and experimental results. *American Mineralogist: Journal of Earth and Planetary Materials*, 102, 1696-1708.

Armstrong, R.A., Compston, W., De Wit, M.J., Williams, I.S., 1990. The stratigraphy of the 3.5-3.2 Ga Barberton Greenstone Belt revisited: a single zircon ion microprobe study. Earth and Planetary Science Letters, 101, 90-106.

Ávila, C.A., Teixeira, W., Cordani, U.G., Moura, C.A.V., Pereira, R.M., 2010. Rhyacian (2.23–2.20 Ga) juvenile accretion in the southern São Francisco craton, Brazil:geochemical and isotopic evidence from the Serrinha magmatic suite, Mineiro belt. J. S. Am. Earth Sci. 29, 464–482.

Ávila, C.A., Teixeira, W., Bongiolo, E.M., Dussin, I.A., 2014. The Tiradentes suite andits role in the Rhyacian evolution of the Mineiro belt-São Francisco Craton: geo-chemical and U-Pb geochronological evidences. Precambrian Research. 243, 221–251.

Babinski, M., Chemale Jr., F., Van Schmus, W.R. 1995. The Pb/Pb age of the Minas Supergoup carbonate rocks, Quadrilátero Ferrífero, Brazil. Precambrian Research, 72, 235–245.

Baltazar, O.F., Zucchetti, M., 2007. Lithofacies associations and structural evolutionof the Archean Rio das Velhas greenstone belt, Quadrilátero Ferrífero, Brazil: a review of the setting of gold deposits. Ore Geology Reviews 32, 1–2.

Barbosa N.S., Teixeira, W., Ávila C.A., Montecinos P.M., Bongiolo E.M., 2015. 2.17–2.10 Ga plutonic episodes in the Mineiro belt, São Francisco Craton, Brazil: U-Pb ages, geochemical constraints and tectonics. Precambrian Research, 270, 204 - 225.

Barbosa, N., Teixeira, W., Ávila, C.A., Montecinos, P.M., Bongiolo, E.M., Vasconcelos, F.F., 2019. U-Pb geochronology and coupled Hf-Nd-Sr isotopic-chemical constraints of the Cassiterita Orthogneiss (2.47–2.41-Ga) in the Mineiro belt, São Francisco craton: Geodynamic fingerprints beyond the Archean-Paleoproterozoic Transition. Precambrian Research, 326, 399-416.Bickle, M. J., Implications of melting for stabilisation of the

lithosphere and heat loss in the Archean, Earth and Planetary Science Letters, 80, 314-324, 1986.

Black, L.P., 1978. The age of the mud tank carbonatite, Strangways range, northern territory. Journal of Australian Geology and Geophysics 3, 227-232.

Black, L.P., Kamo, S.L., Allen, C.M., Aleinikoff, J.N., Davis, D.W., Korsch, R.J., Foudoulis,C., 2003. TEMORA 1 a new zircon standard for Phanerozoic U–Pb geochronology. Chemical Geology 200, 155–170.

Blichert-Toft, J., Puchtel, I.S., 2010. Depleted mantle sources through time: evidence from Lu–Hf and Sm–Nd isotope systematics of Archean komatiites. Earth and Planetary Science Letters 297 (3–4), 598–606.

Bouvier, A., Vervoort, J.D., Patchett, P.J., 2008. The Lu-Hf and Sm-Nd isotopic com-position of CHUR: constraints from unequilibrated chondrites and implications for the bulk composition of terrestrial planets. Earth and Planetary Science Letters 273, 48-57.

Boynton,W.V., 1984. Cosmochemistry of the rare earth elements: meteorite studies. In: Henderson, P. (Ed.), Rare Earth Element Geochemistry (Developments in Geochemistry 2). Elsevier, Amsterdam, pp. 63e114.

Brown, M., Johnson, T., 2018. Secular change in metamorphism and the onset of global plate tectonics. American Mineralogist, 103(2), pp.181-196.

Carvalho, B.B., Janasi, V.A., Sawyer, E.W., 2017. Evidence for Paleoproterozoic anatexis and crustal reworking of Archean crust in the São Francisco Craton, Brazil: a dating and isotopic study of the Kinawa migmatite. Precambrian Research, 291, 98-118.

Carneiro, M. A., 1992. O complexo Metamórfico do Bonfim Setentrional. Revista da Escola de Minas, Universidade Federal de Ouro Preto, Ouro Preto (Brazil) 45, 155–156.

Chemale Jr., F., Rosière, C.A., Endo, I., 1994. The tectonic evolution of the Quadrilátero Ferrífero, Minas Gerais, Brazil. Precambrian Research, 65, 25–54.

Cherniak, D.J., 2000. Pb diffusion in rutile. Contributions to Mineralogy and Petrology, 139(2), 198-207.

Cherniak, D.J., Manchester, J. and Watson, E.B., 2007. Zr and Hf diffusion in rutile. Earth and Planetary Science Letters, 261(1-2), 267-279.

Corfu, F., Hanchar, J.M., Hoskin, P.W.O., Kinny, P., 2003. Atlas of zircon textures. In:Hanchar, J.M., Hoskin, P.W.O. (Eds.), Zircon, Reviews in Mineralogy & Geochemistry.Mineralogical Society of America 53, 468–500.

Cutts, K., Lana, C., Alkmim, F., Farina, F., Moreira, H., Coelho, V. 2019. Metamorphism and exhumation of basement gneiss domes in the Quadrilátero Ferrífero: two stage dome-and-keel evolution? *Geoscience Frontiers.* doi.org/10.1016/j.gsf.2019.02.009

da Fonseca, G.M., Jordt-Evangelista, H., Queiroga, G.N., 2018. Petrogenesis of metaultramafic rocks from the Quadrilátero Ferrífero and adjacent terrains, Minas Gerais, Brazil: Two events of ultramafic magmatism? Journal of South American Earth Sciences, 82, 16-32.

Dorr II, J.V.N., 1969. Physiographic, Stratigraphic and Structural Development of the Quadrilátero Ferrífero, Minas Gerais, Brazil. USGS/DNPM, Washington, Prof.Paper 641-A, 110 pp.

Dhuime, B., Hawkesworth, C. and Cawood, P., 2011. When continents formed. Science, 331.6014,154-155.

Ewing, T.A., Hermann, J., Rubatto, D., 2013. The robustness of the Zr-in-rutile and Ti-in-zircon thermometers during high-temperature metamorphism (Ivrea-Verbano Zone, northern Italy). Contributions to Mineralogy and Petrology, 165, 757-779.

Farina, F., Albert, C., Lana, C., 2015. The Neoarchean transition between medium- and high-K granitoids: Clues from the Southern São Francisco Craton (Brazil). Precambrian Research, 266, 375 – 394.

Ferry, J.M., Watson, E.B., 2007. New thermodynamic models and revised calibrations for the Ti-in-zircon and Zr-in-rutile thermometers. Contributions to Mineralogy and Petrology, 154, 429-437.

Foley, S.F., Buhre, S., Jacob, D.E., 2003. Evolution of the Archaean crust by delamination and shallow subduction. Nature, 421(6920), p.249.

Fu, B., Page, F.Z., Cavosie, A.J., Fournelle, J., Kita, N.T., Lackey, J.S., Wilde, S.A., Valley, J.W., 2008. Ti-in-zircon thermometry: applications and limitations. Contributions to Mineralogy and Petrology 156, 197–215.

Gerdes, A., Zeh, A., 2006. Combined U–Pb and Hf isotope LA-(MC-)ICP-MS analyses of detrital zircons: comparison with SHRIMP and new constraints for the provenance and age of an Armorican metasediment in central Germany. Earth and Planetary Science Letters 249, 47–61.

Gerdes, A., Zeh, A., 2009. Zircon formation versus zircon alteration – new insights from combined U–Pb and Lu–Hf in situ LA-ICP-MS analyses, and consequencesfor the interpretation of Archean zircon from the Limpopo Belt. Chemical Geology 261,230–243.

Goodge, J.W., Vervoort, J.D., 2006. Origin of Mesoproterozoic A-type granites in Laurentia: Hf isotope evidence. Earth and Planetary Science Letters 243, 711-731.

Grant, M.L., Wilde, S.A., Wu, F.Y., Yang, J.H., 2009. The application of zircon cathodoluminescence imaging, The U-Pb chemistry and U-Pb ages in interpreting discrete magmatic and high-grade metamorphic events in the North China Craton at the Archean/Proterozoic boundary. Chemical Geology 261, 155-171.

Griffin, W.L., Wang, X., Jackson, S.E., Pearson, N.J., O'Reilly, S.Y., Xu, X., Zhou, X. 2002. Zircon chemistry and magma mixing, SE China: In situ analysis of Hf isotopes, Tonglu and Pingtan igneous complexes. Lithos, 61, 237-269.

Guillong, M., Meier, D.L., Allan, M.M., Heinrich, C.A., Yardley, B.W., 2008. Appendix A6: SILLS: A MATLAB-based program for the reduction of laser ablation ICP-MS data of homogeneous materials and inclusions. Mineralogical Association of Canada Short Course, 40, 328-333.

Guitreau, M., 2012. Les isotopes de l'Hafnium dans les TTG et leurs zircons: témoins de la croissance des premiers continents Unpublished PhD Thesis École Normale Supérieure de Lyon, France.

Guo, S., Tang, P., Su, B., Chen, Y., Ye, K., Zhang, L., Gao, Y., Liu, J., Yang, Y., 2017. Unusual replacement of Fe-Ti oxides by rutile during retrogression in amphibolite-hosted veins (Dabie UHP terrane): A mineralogical record of fluid-induced oxidation processes in exhumed UHP slabs. American Mineralogist, 102(11), 2268-2283.

Harley, S.L., Kelly, N.M., Möller, A., 2007. Zircon behaviour and the thermal histories of mountain chains. Elements 3 (1), 25–30.

Hawkesworth, C., Cawood, P., Dhuime, B., 2016. Tectonics and crustal evolution. GSA Today. 26, 4 – 11. doi: 10.1130/GSATG272A.1.

Hartmann, L.A., Endo, I., Suita, M.T.F., Santos, J.O.S., Frantz, J.C., Carneiro, M.A., Naughton, N.J., Barley, M.E., 2006. Provenance and age delimitation of Quadrilátero Ferrífero sandstones based on zircon U–Pb isotopes. Journal of South American Earth Sciences 20, 273–285.

Heilbron, M., Duarte, B.P., Valeriano, C.M., Simonetti, A., Machado, N., Nogueira, J.R., 2010. Evolution of reworked Paleoproterozoic basement rocks within the Ribeira belt (Neoproterozoic), SE-Brazil, based on U–Pb geochronology: Implications for paleogeographic reconstructions of the São Francisco-Congo paleocontinent. Precambrian Research, 178, 136–148.

Heilbron, H., Cordani, U., Alkmim, F., Reis, H., 2017. Tectonic Genealogy of a Miniature Continent. In: Heilbron, M., Cordani, U.G., Alkmim, F.F. (Eds.), São Francisco Craton, Eastern Brazil. Regional Geology Reviews. Springer, Cham. 321-331.Herz, N., 1978. Metamorphic rocks of the Quadrilátero Ferrífero, Minas Gerais, Brazil. U.S. Geological.Survey Professional Paper, 641-C, 81p.

Jackson, S.E., Pearson, N.J., Griffin, W.L., Belousova, E.A., 2004. The application of laserablation-inductively coupled plasma-mass spectrometry to in situ U–Pb zircon geochronology. Chemical Geology 211, 47–69.

Jaupart, C., Mareschal, J.C., 2015. Post-orogenic thermal evolution of newborn Archean continents. Earth and Planetary Science Letters 432, 36–45.

Jordt-Evangelista, H., Alkmim, F.F.,Marshak, S., 1992. Metamorfismo progressivo e a ocorrência dos 3 polimorfos $Al_2O_3SiO_5$ (cianita, andaluzita e sillimanita) na Formação Sabará em Ibirité, Quadrilátero Ferrífero, MG. Revista da Escola de Minas, 45(1/2), 157–160.

Kamber, B.S., 2015. The evolving nature of terrestrial crust from the Hadean, through the Archaean, into the Proterozoic. Precambrian Research 258, 48-82.

Kelly, N.M., Harley, S.L., 2005. An integrated microtextural and chemical approach to zircon geochronology: refining the Archaean history of the Napier Complex, east Antarctica. Contributions to Mineralogy and Petrology, 149(1), pp.57-84.

Koglin, N., Zeh, A., Cabral, A.R., Gomes Jr., A.A.S., Neto, A.V.C., Brunetto, W.J., Galbiatti, H., 2014. Depositional age and sediment source of the auriferous Moeda Formation, Quadrilátero Ferrífero of Minas Gerais Brazil: new constraints from U-Pb–Hf isotopes in zircon and xenotime. Precambrian Research 255, 96–108.

Kohn, M.J., 2017. Titanite petrochronology. Reviews in Mineralogy and Geochemistry, 83(1), 419-441.

Korhonen, F.J., Clark, C., Brown, M., Taylor, R.J.M., 2014. Taking the temperature of Earth's hottest crust. Earth and Planetary Science Letters, 408, 341-354.

Kröner, A., Wan, Y., Liu, X., Liu, D.Y., 2014. Dating of zircons from high-grade rocks:which is the most reliable method? Geoscience Frontiers 5, 515–523.

Kusky, T.M., Polat, A., 1999. Growth of granite-greenstone terranes at convergent margins, and stabilization of Archean cratons. Tectonophysics 305, 43–73.

Kunz, B.E., Regis, D., Engi, M., 2018. Zircon ages in granulite facies rocks: decoupling from geochemistry above 850° C? Contributions to Mineralogy and Petrology, 173, 26.

Lana, C., Alkmim, F. F., Armstrong, R., Scholz, R., Romano, R. & Nalini Jr., H. A., 2013. The ancestry and magmatic evolution of Archean TTG rocks of the Quadrilátero Ferrífero province, southeast Brazil. Precambrian Research, 231, 157–173.

Ludwig, K.R., 2003. ISOPLOT/Ex, version 3, A Geochronological Toolkit for Microsoft Excel. Berkeley Geochronology Center. Special Publication 4, 71.

Luvizotto, G.L., Zack, T., Meyer, H.P., Ludwig, T., Triebold, S., Kronz, A., Münker, C., Stockli, D.F., Prowatke, S., Klemme, S., Jacob, D.E., von Eynatten, H., 2009a. Rutile crystals as potential trace element and isotope mineral standards for microanalysis. Chemical Geology 261, 346–369.

Luvizotto, G.L., Zack, T., Triebold, S., Von Eynatten, H., 2009b. Rutile occurrence and trace element behavior in medium-grade metasedimentary rocks: example from the Erzgebirge, Germany. Mineralogy and Petrology, 97(3-4), 233-249.

Machado, N., Carneiro, M., 1992. U–Pb evidence of late Archean tectono-thermal activity on the southern São Francisco shield, Brazil. Canadian Journal of Earth Sciences, 29 (11), 2341 – 2346.

Marshak, S., Tinkham, D., Alkmim, F., Brueckner, H. and Bornhorst, T., 1997. Dome-and-keel provinces formed during Paleoproterozoic orogenic collapse-core complexes, diapirs, or neither?: examples from the Quadrilátero Ferrífero and the Penokean orogen. Geology, 25. 415-418.

Martínez Dopico, M.I., Lana, C., Moreira, H.S., Cassino, L.F., Alkmim, F.F., 2017. U-Pb ages and Hf-Isotope data of detrital zircons from the late Neoarchean-Paleoproterozoic Minas Basin, SE Brazil. Precambrian Research. 291, 143–161.

Meinhold, G., Anders, B., Kostopoulos, D., Reischmann, T., 2008. Rutile chemistry and thermometry as provenance indicator: an example from Chios Island, Greece. Sedimentary Geology, 203(1-2), 98-111.

Mendes, M.C.O., Lobato, L.M., Suckau, V., Lana, C., 2014. In situ LA-ICPMS U–Pb dating of detrital zircons from the Cercadinho Formation, Minas Supergroup. Revista do Instituto de Geociências – USP 14 (1), 55–68.

Meert, J.G., 2012. What's in a name? The Columbia (Paleopangaea/Nuna) supercontinent. Gondwana Research 21, 987–993.

Moreira, H., Lana, C., Nalini Jr., H.A., 2016. The detrital zircon record of an Archaean convergent basin in the Southern São Francisco Craton, Brazil. Precambrian Research 275, 84–99.

Moreira, H., Seixas, L., Storey, C., Fowler, M., Lasalle, S., Stevenson, R., Lana, C., 2018. Evolution of siderian juvenile crust to rhyacian high Ba-Sr magmatism in the Mineiro Belt, southern São Francisco Craton. Geoscience Frontiers, 9(4), 977-995.Nasdala, L., Gotze, J., Pidgeon, R.T., Kempe, U., Seifert, T., 1998. Constraining a SHRIMP U-Pb age: micro-scale characterization of zircons from Saxonian Rotliegend rhyolites. Contributions to Mineralogy and Petrology 132, 300–306. doi:10.1007/s004100050423

Noce, C.M., Teixeira, W., Quéméneur, J.J.G., Martins, V.T.S., Bolzachini, E., 2000. Isotopic signatures of Paleoproterozoic granitoids from southern São Francisco Craton, NE Brazil, and implications for the evolution of the Transamazonian Orogeny. Journal of South Amercian Earth Sciences 13, 225–239.

Noce, C.M., Zuccheti, M., Baltazar, O.F., Armstrong, R., Dantas, E., Renger, F.E., Lobato, L.M., 2005. Age of felsic volcanism and the role of ancient continental crust in the evolution of the Neoarchean Rio das Velhas Greenstone belt (Quadrilátero Ferrífero, Brazil): U–Pb zircon dating of volcaniclastic graywackes. Precambrian Research, 141, 67–82.

Paton, C., Hellstrom, J., Paul, B., Woodhead, J., Hergt, J., 2011. Iolite: freeware for the visualisation and processing of mass spectrometric data. Journal of Analytical Atomic Spectrometry 26, 2508. http://dx.doi.org/10.1039/c1ja10172b.

Payne, J.L., McInerney, D.J., Barovich, K.M., Kirkland, C.L., Pearson, N.J., Hand, M., 2016. Strengths and limitations of zircon Lu-Hf and O isotopes in modelling crustal growth. Lithos 248-251, 175–192.

Pearson, D.G., Snyder, G.A., Shirey, S.B., Taylor, L.A., Carlson, R.W., Sobolev, N.V., 1995. Archaean Re–Os age for Siberian eclogites and constraints on Archaean tectonics. Nature, 374(6524), 711.

Peucat, J.J., Hirata, T., Nesbitt, R.W., 1995. REE fractionation (ICPMS LASER) evidence in metamorphic zircons during granulite facies metamorphism and anatectic processes. Terra Abstracts 7, 346.

Piazolo, S., Belousova, E., La Fontaine, A., Corcoran, C., Cairney, J.M., 2017. Trace element homogeneity from micron- to atomic scale: Implication for the suitability of the zircon GJ-1 as a trace element reference material. Chemical Geology 456, 10–18.

Pires, F. R. M. 1995. Textural and mineralogical variations during metamorphism of the Proterozoic Itabira Iron Formation in the Quadrilátero Ferrífero, Minas Gerais, Brazil. Anais da Academia Brasileira de Ciências, 67(1), 77–105.

Polat, A., Wang, L., Appel, P.W.U., 2015. A review of structural patterns and melting processes in the Archean craton of West Greenland: Evidence for crustal growth at convergent plate margins as opposed to non-uniformitarian models. Tectonophysics 662, 67-94

Reis, L.A., Martins-Neto, M.A., Gomes, N.S., Endo, I., 2002. A bacia de antepaís paleoproterozóica Sabará, Quadrilátero Ferrífero, MG. Revista Brasileira de Geociências 32, 43-58.

Reimink, J.R., Davies J., Chacko T., Stern R.A., Heaman L.M., Sarkar C., Schaltegger U., Creaser R. A., Pearson D.G. 2016. No evidence for Hadean continental crust within Earth's oldest evolved rock unit. Nature Geosciences 9. 777–780.

Renger, F.E., Noce, C.M., Romano, A.W., Machado, N., 1995. Evolução sedimentar do Supergrupo Minas: 500 Ma de registro geológico no Quadrilátero Ferrífero, Minas Gerais, Brasil. Geonomos, 2 (1), 1–11.

Romano, R., Lana, C., Alkmim, F.F., Stevens, G.S., Armstrong, R., 2013. Stabilization of the southern portion of the São Francisco Craton, SE Brazil, through a long-lived period of potassic magmatism. Precambrian Research 224, 143–159.

Rosière CA, Chemale F Jr. Itabiritos e minérios de ferro de alto teor do Quadrilátero Ferrífero: uma visão geral e discussão. Geonomos. 2000; 8 (2):27-43.

Rubatto, D., 2017. Zircon: the metamorphic mineral. Reviews in Mineralogy and Geochemistry, 83, 261-295.

Rubatto, D., Gebauer, D., Compagnoni, R., 1999. Dating of eclogite-facies zircons: the age of Alps metamorphism in the Sesia-Lanzo Zone (Western Alps). Earth and Planetary Science Letters 167, 141–158.

Rubatto, D., 2002. Zircon trace element geochemistry: partitioning with garnet and the link between U–Pb ages and metamorphism. Chemical Geology, 184, 123-138.

Rubatto, D., Hermann, J., 2007a. Zircon behaviour in deeply subducted rocks. Elements, 3(1), 31-35.

Rubatto, D. and Hermann, J., 2007b. Experimental zircon/melt and zircon/garnet trace element partitioning and implications for the geochronology of crustal rocks. Chemical Geology, 241(1-2), 38-61.

Santos, M.M., Lana, C., Scholz, R., Buick, I., Schmitz, M.D., Kamo, S.L., Gerdes, A., Corfu, F., Tapster, S., Lancaster, P., Storey, C.D., 2017. A new appraisal of Sri Lankan BB zircon as a reference material for LA-ICP-MS U-Pb geochronology and Lu-Hf isotope tracing. Geostandards and Geoanalytical Research 41, 335-358.

Santosh, M., Wan, Y.S., Liu, D.Y., Dong, C.Y., Li, J.H., 2009. Anatomy of zircons from an ultra-hot orogen: the amalgamation of the North China Craton within the supercontinent Columbia. The Journal of Geology 117, 429-443.

Schaltegger, U., Fanning, C.M., Gunther, D., Maurin, J.C., Schulmann, K., Gebauer, D., 1999. Growth, annealing and recrystallization of zircon and preservation of monazite in high-grade metamorphism: conventional and in-situ U–Pb isotope, cathodoluminescence and microchemical evidence. Contributions to Mineralogy and Petrology 134, 186-201.

Schmitt, A.K., Zack, T., 2012. High-sensitivity U–Pb rutile dating by secondary ion mass spectrometry (SIMS) with an O2+ primary beam. Chemical Geology, 332, 65-73.

Seixas, L.A.R., David, J., Stevenson, R., 2012. Geochemistry, Nd isotopes and U–Pb geochronology of a 2350 Ma TTG suite, Minas Gerais, Brazil: Implications for the crustal evolution of the southern São Francisco craton. Precambrian Research.196–197, 61–80.

Seixas, L.A.R., Bardintzeff, J-M., Stevenson, R., Bonin, B., 2013. Petrology of the high-Mg tonalites and dioritic enclaves of the ca.2130 Ma Alto Maranhão suite:evidence for a major juvenile crustal addition event during the Rhyacian orogenesis, Mineiro Belt, southeast Brazil. Precambrian Research. 238, 18–41.

Sláma, J., Košler, J., Condon, D.J., Crowley, J.L., Gerdes, A., Hanchar, J.M., Horstwood, M.S.A., Morris, G.A., Nasdala, L., Norberg, N., Schaltegger, U., Schoene, B., Tubrett,M.N., Whitehouse, M.J., 2008. Plešovice zircon – a new natural reference material for U–Pb and Hf isotopic microanalysis. Chemical Geology 249, 1–35.

Takenaka, L., Lana, C., Scholz, R., Nalini Jr., H.A., Abreu, A.T., 2015. Optimization of the in-situ U–Pb age dating method via LA-Quadrupole ICP-MS with applications to the timing of U–Zr–Mo mineralization in the Poçosde Caldas Alkaline Complex, SE Brazil. Journal of South Amercian Earth Sciences 62, 70–79.

Taylor, R.J.M., Harley, S.L., Hinton, R.W., Elphick, S., Clark, C. and Kelly, N.M., 2015. Experimental determination of REE partition coefficients between zircon, garnet and melt: a key to understanding high-T crustal processes. Journal of Metamorphic Geology, 33(3), 231-248.Taylor, R. J. M., Kirkland, C. L., Clark, C., 2016. Accessories after the facts: Constraining the timing, duration and conditions of high-temperature metamorphic processes. Lithos, 264, 239–257.

Taylor, R.J.M., Clark, C., Harley, S.L., Kylander-Clark, A.R.C., Hacker, B.R., Kinny, P.D., 2017. Interpreting granulite facies events through rare earth element partitioning arrays. Journal of Metamorphic Geology. 35:759–775.

Teixeira, W., Carneiro, M.A., Noce, C.A., Machado, N., Sato, K., Taylor, P.N., 1996. Pb, Sr and Nd isotope constraints on the Archean evolution of gneissic granitoid complexes in the southern São Francisco Craton, Brazil. Precambrian Research 78,151–164.

Teixeira, W., Ávila, C.A., Dussin, I.A., Corrêa Neto, A.V., Bongiolo, E.M., Santos, J.O.,Barbosa, N.S., 2015. A juvenile accretion episode (2.35–2.32 Ga) in the Mineiro Belt and its role to the Minas accretionary orogeny: Zircon U–Pb–Hf and geochemical evidences. Precambrian Research, 256, 148–169.

Teixeira, W., Oliveira, E.P. and Marques, L.S., 2017. Nature and evolution of the Archean crust of the São Francisco Craton. In São Francisco Craton, Eastern Brazil. Springer, Cham. 29-56.Tomkins, H.S., Powell, R., Ellis, D.J., 2007. The pressure dependence of the zirconium-in-rutile thermometer. Journal of Metamorphic Geology, 25(6), 703-713.

van Achterbergh, E., Ryan, C.G., Jackson, S.E., Griffin, W., 2001. Appendix III. Data reduction software for LAICP-MS. In: Sylvester, P. (Ed.), Laser-ablation-ICP-MS in the Earth sciences, principles and applications. Mineralogical Association of Canada. Short Course Series 29, pp. 239–243.

Vavra, G., Gebauer, D., Schmid, R. and Compston, W., 1996. Multiple zircon growth and recrystallization during polyphase Late Carboniferous to Triassic metamorphism in granulites of the Ivrea Zone (Southern Alps): an ion microprobe (SHRIMP) study. Contributions to Mineralogy and Petrology, 122(4), 337-358.Verma, S.K., Oliveira, E.P., Silva, P.M., Moreno, J.A., Amaral, W.S., 2017. Geochemistry of komatiites and basalts from the Rio das Velhas and Pitangui greenstone belts, São Francisco Craton, Brazil: Implications for the origin, evolution, and tectonic setting. Lithos, 284, 560-577.

Vervoort, J.D. and Kemp, A.I.S, 2016. Clarifying the zircon Hf isotope record of crust–mantle evolution. Chemical Geology 425, 65-75.

Vial, D.S., Abreu, G.C., Schubert, G., Ribeiro-Rodrigues, L.C., 2007. Smaller gold deposits in the Archean Rio das Velhas greenstone belt, Quadrilátero Ferrífero, Brazil. Ore Geology Reviews, 32, 651-673.

Wan, Y.S., Liu, D.Y., Dong, C.Y., Xu, Z.Y., Wang, Z.J., Wilde, S.A., Yang, Y.H., Liu, Z.H., Zhou, H.Y., 2009. The Precambrian Khondalite Belt in the Daqingshan area, North China Craton: evidence for multiple metamorphic events in the Palaeoproterozoic era. In: Reddy, S.M., Mazumder, R., Evans, D.A.D., Collins, A.S. (Eds.), Palaeoproterozoic Supercontinents and Global Evolution. Geological Society, London, Special Publication, 323, pp. 73-97.

Wan, Y.S., Liu, D.Y., Dong, C.Y., Liu, C.J., Wang, S.J., Yang, E.X., 2011. U-Th-Pb behavior of zircons under high-grade metamorphic conditions: a case study of zircon dating of meta-diorite near Qixia, eastern Shandong. Geoscience Frontiers 2, 137–146.

Watson, E.B., Wark, D.A., Thomas, J.B., 2006. Crystallization thermometers for zircon and rutile. Contributions to Mineralogy and Petrology, 151, 413.

Whitehouse, M.J., Kemp, A.I.S., 2010. On the difficulty of assigning crustal residence, magmatic protolith and metamorphic ages to Lewisian granulites: constraints from combined in situ U–Pb and Lu–Hf isotopes. Geological Society, London, Special Publications, 335(1), pp.81-101.

Wiedenbeck, M., Alle, P., Corfu, F., Griffin, W.L., Meier, M., Oberli, F., Quadt, A.V., Roddick, J.C., Spiegel, W., 1995. Three natural zircon standards for U–Th–Pb, Lu–Hf, trace element and REE analyses. Geostandards and Geoanalytical Research 19, 1–23.

Woodhead, J.D., Hergt, J.M., 2005. Preliminary appraisal of seven natural zircon reference materials for in situ Hf isotope determination. Geostandards and Geoanalytical Research 29, 183–195.

Wu, F.-Y., Yang, Y.-H., Xie, L.-W., Yang, J.-H., Xu, P., 2006. Hf isotopic compositions of the standard zircons and baddeleyites in U–Pb geochronology. Chemical Geology 234, 105–126.

Yakymchuk, C., Kirkland, C.L. and Clark, C., 2018. Th/U ratios in metamorphic zircon. Journal of Metamorphic Geology, 36(6), 715-737. Zack, T., Moraes, R., Kronz, A., 2004. Temperature dependence of Zr in rutile: empirical calibration of a rutile thermometer. Contributions to Mineralogy and Petrology 148(4) 471-488.

Zack, T., Kooijman, E., 2017. Petrology and geochronology of rutile. Reviews in Mineralogy and Geochemistry, 83(1), 443-467.

Zack, T., Kronz, A., Foley, S.F., Rivers, T., 2002. Trace element abundances in rutiles from eclogites and associated garnet mica schists. Chemical Geology, 184(1-2), 97-122.

Zack, T., Stockli, D.F., Luvizotto, G.L., Barth, M.G., Belousova, E., Wolfe, M.R., Hinton, R.W., 2011. In situ U–Pb rutile dating by LA-ICP-MS: 208 Pb correction and prospects for geological applications. Contributions to Mineralogy and Petrology, 162(3), 515-530.

Figure captions

Figure 1: A) Map overview of the São Francisco Craton inset and possible boundary along principal belts during the Palaeoproterozoic orogeny and later Neoproterozoic belt (modified from Heilbron et al., 2010; Alkmim and Martins-Neto, 2012); B) Geological map of the Southern São Francisco Craton comprising principal domains and rock units of the region. The craton contour and metamorphic constraints are also indicated. This entire area was thermal-tectonically affected during the Palaeoproterozoic. The extension of this overprint is still poorly understood (modified from Alkmim and Marshak, 1998; Seixas et al. 2012; Romano et al., 2013; Lana et al., 2013; Teixeira et al., 2015; Alkmim and Teixeira, 2017).

Figure 2: A) Detailed geological map of the study area showing main lithological units and sample localities. Zircon compilation ages of the Bação Complex and Santa Rita dome from Lana et al. (2013). Titanite age of the Bação Complex Cutts et al. (2019). Schematic section along the Dom Bosco synform (keel). The section is vertically exaggerated and shows the intricate arrangement of the Minas and Rio das Velhas supracrustal units, related to the doming event in the Palaeoproterozoic and to thrusting during the east-west convergence in the Brasiliano (see text for details). B) Stratigraphic column of the supracrustal sequences of the Quadrilátero Ferrífero. References to the age data are listed in the figure by the numbers in parentheses. With exception of Babinski et al. (1995), the compilation of ages come from zircon U-Pb studies.

Figure 3: Field photographs of the felsic intrusions in the Minas and Rio das Velhas supergroups. A) Felsic intrusion A2. The intrusive contact is highlighted by the dashed lines and the host schist foliation (Sn) by straight lines; B) Samples B1a (schist) and B2a (felsic intrusion). The foliation in the schist (Sn) is indicated by straight lines; C) Detail of intrusive contact between felsic intrusion A2 and its host schist. Small elongated blobs are found sub parallel to the schist foliation suggesting a syn-genetic relationship; D) Felsic intrusion B2b depicting folds and faults (hammer for scale); E) Outcrop scale exposing the concordant to sub-concordant felsic layer overlying a set of itabirites in the Ouro Preto ridge; F) Intrusion C1 extracted next to the contact with itabirites. The contact (dashed lines) is parallel to the itabirites schistosity.

Figure 4: A) Concordia and relative age distribution diagrams of U-Pb ages from sample A1. This intrusion has crystallisation age at around 2947 Ma and an inherited group of zircon grains that range from 3100 to 3300 Ma; CL images of zircon grains, U-Pb spots and $^{207}Pb/^{206}Pb$ ages are indicated. Analyses are concordant or sub-concordat, otherwise indicated by degree of concordance in percentage; B) Concordia and relative age distribution diagrams of U-Pb analyses for sample A2. This intrusion crystallised at 2827 Ma and an inherited population of zircon grains yield an intercept age of 3198 Ma. CL images of zircon grains and respective U-Pb spots are also presented. Both samples have relatively bigger, dark and prismatic zircon grains, which yielded the youngest ages.

Figure 5: A) Concordia age for crystallisation of sample B2a at 2127 Ma (upper left corner). The sample contained a number of round, complexly zoned zircon grains that are older than 2680 Ma. U-Pb-Hf analyses of one of them, zircon Zr44, is given in the lower right corner; B) Cathodoluminescence image of zircon Zr14. U–Pb–Hf measurement spots are indicated.

Figure 6: Cathodoluminescence image of the general features of the 'soccer ball' zircons found in schist sample B1a from the Rio das Velhas Greenstone belt sequence**.** Note the general manifold zoning and the systematic shape and size of the grains. Sector and fir-tree zoning are common features. The majority of them has a dark core surrounded by a lighter rim and a bleaching transition is common. U–Pb, Lu–Hf and trace element measurement spots are indicated. U-Pb analyses of multiple domains are highly concordant. Data listed by spot numbers are available in the supplementary data file.

Figure 7: A) Concordia diagram showing concordant analyses of zircons from schist sample B1a. Purple and red analyses were performed at UFOP, grey analyses were done at UoP. Inset: histogram showing the age distribution for both cores and rims analyses. A number of spots on the rims suggest a metamorphic overprint towards c. 2700 Ma. Cores depict main peak of ages at c. 2940 Ma, and rims show main peak at 2690 Ma (UFOP). Perfectly euhedral soccer ball grains show peak at 2730 Ma (UoP). B) Concordia Intercept age for rutile grains of sample B1a at 2172 ± 33 Ma. Older grains were omitted in this plot but are presented in the weighted mean average. Archaean and Palaeoproterozoic rutiles show no morphological distinction and yield same temperature (c. 735 °C) in the Zr-thermometry of Ferry and Watson (2007) (see text for explanation).

Figure 8: A) Concordia diagram showing concordant analyses of magmatic zircons for sample B2b and concordia intercept age of youngest cluster of $^{207}Pb/^{206}Pb$ at 2135 Ma. The sample contains a number of transparent, euhedral prismatic zircons, marked by sector zoning under cathodoluminescence. B) Cathodoluminescence image of multiple U-Pb analyses on single grain followed by their weighted mean average age of 2125 Ma.

Figure 9: A) Concordia diagram of sample B2c U-Pb zircon analyses. Probability density curve for the $^{207}Pb/^{206}Pb$ Archaean ages is shown in the upper left corner. Intercept age of the youngest group of U-Pb ages also presented. B) Cathodoluminescence image of prismatic-elongated zircons along with U-Pb ages. Note the large size and magmatic zoning of the grains.

Figure 10: Concordia intercept age of sample C1 (lower right corner) and probability density diagrams of $^{207}Pb/^{206}Pb$ zircon ages (upper left corner).

Figure 11: A) $^{176}Hf/^{177}Hf$t versus apparent $^{207}Pb/^{206}Pb$ age diagrams for analysed zircons from sample B2a (green dots) and sample B1a (purple for cores and red for rims). Three core-rim analysed zircons are connected by straight lines. Grey arrow indicates Pb loss trend. Yellow transparent spots are from Barbosa et al., 2015. Vertical bars indicate Rio das Velhas (RV I), Rio das Velhas (RV II) and Mamona

magmatic events (Lana et al., 2013, Farina et al., 2015) and the Minas accretionary orogeny (Teixeira et al., 2015), respectively. This diagram shows the evolution of the Hf systematics with time from the Archaean to Palaeoproterozoic (see text for more details). B) Diagram of $\varepsilon Hf_{(t)}$ against $^{207}Pb/^{206}Pb$ ages. Green dots represent felsic intrusion zircons (sample B2a). Purple and red dots depict cores and rims analyses of zircons from sample B1a, respectively. The large arrow shows a crustal evolution of Archaean-Proterozoic zircons calculated using a crustal $^{176}Lu/^{177}Hf = 0.015$ (Goodge and Vervoort, 2006; Griffin et al., 2002; Dhuime et al., 2011). Red areas represent the specific $\varepsilon Nd_{(t)}$ signature of plutonic rocks of the Mineiro Belt – Resende Costa (RC); Lagoa Dourada (LD); Alto Maranhão (AM); Ritápolis (R); Represa de Camargos (RdC); Serrinha e Tiradentes (S&T) (Noce et al., 2000; Ávila et al., 2010, 2014; Seixas et al., 2012, 2013; Teixeira et al., 2015; Barbosa et al., 2015). Yellow squares are from Teixeira et al. (2015) and correspond to in situ Lu-Hf zircon analyses of Resende Costa orthogneiss and Restinga de Baixo amphibolite. Red and purple squares are from Moreira et al. (2018) and represent in situ Lu-Hf zircon analyses from AM and LD suites. Depleted Mantle area (DM) after Guitreau 2012 and Albert et al. 2016. CHUR constants of Bouvier et al. (2008; $^{176}Hf/^{177}Hf = 0.282785$ and $^{176}Lu/^{177}Hf = 0.0336$) and T_{DM} constants (lighter straight line on the background) of Amelin et al. (2000) and Griffin et al. (2000) ($^{176}Hf/^{177}Hf = 0.283165$ and $^{176}Lu/^{177}Hf = 0.0384$). For comparison, T_{DM} calculations using the $^{176}Lu/^{177}Hf$ and $^{176}Hf/^{177}Hf$ ratios of 0.03933 and 0.283294 (Blichert-Toft and Puchtel, 2010) are presented in the supplementary material. Vertical bars indicate Rio das Velhas I (RV I), Rio das Velhas II (RV II) and Mamona magmatic events.

Figure 12: A) Chondrite normalized REE elements of zircons from sample B1a (chondrite values from Boynton, 1984). They are divided in two groups based on the relative flatness and concentration of the MREE - HREE. The group with flat HREE have limited Ti variation and maximum values up to 25 ppm. The variable degree of fractionation in the second group suggests a domainal garnet controlling REE concentration; B) Ti concentration of the different zircons versus $^{207}Pb/^{206}Pb$ ages and $\varepsilon Hf_{(t)}$ values when available.

Table 1: Summary of U-Pb analyses of zircons from felsic intrusions. The symbol (n) represents the number of analyses utilised for Concordia/Intercept ages calculation; the asterisk represents the number of grains with two or more analyses each; c – core; r – rim analysis. U-Pb analyses in rutiles from schist sample B1a are also presented for comparison. Detrital inherited zircons from the same schist sample were omitted. [a]Intercept age obtained from rutile grains with essentially radiogenic Pb (not corrected).[b] Intercept age after common Pb correction. [c]Intercept age from corrected ages of grains with common ^{206}Pb <0.2%.

Sample	Number of zircon analyses	Conc. / Sub-Conc. analyses (>98%)	Youngest concordant zircon age (Ma)	Concordia / Intercept Crystallisation. Age in Ma (n)	Concordia / Intercept Inherited age in Ma (n)	Zircon size range (μm) (average size)
A1	53 - 1*	34	2921 ± 36	2949 ± 6 (15);	3121 ± 7 (7)	95 - 500 (250)
A2	30 - 2*	22	2820 ± 40	2827 ± 7 (8);	3201 ± 6 (15)	75 – 450 (200)
B2a	24 - 2*	22	2122 ± 42	2127 ± 6 (14);	2936 ± 40c; 2718 ± 54r	100 – 505 (250)
B2b	46 - 4*	37	2086 ± 30	2135 ± 16 (36);	2912 ± 21c; 2778 ± 19r	200 – 610 (300)
B2c	50	27	2065 ± 27	2133 ± 28 (14);	3177 ± 17 - 2697 ± 19	200 – 705 (300)
C1	13	11	2093 ± 36	2130 ± 30 (7);	3363 ± 17; 2688 ± 17	100 – 405 (325)
	Number of rutile analyses	**Conc. / Sub-Conc. analyses (>98%; < 102%)**	**Youngest concordant rutile age (Ma)**	**Intercept age in Ma (n)**	**Inherited age in Ma (n)**	**Rutile size range (μm) (average size)**
B1a	19 – 3*	4	2118 ± 42	2173 ± 27[a] 2137 ± 29[b] 2172 ± 33[c]	c. 2600 Ma (2)	50 – 500 (300)

Highlights

Archaean felsic intrusions constrain the Rio das Velhas Greenstone Belt evolution in at least 200 Myr;

High-grade soccer ball metamorphic zircon grains depict conditions of Archaean crustal amalgamation;

First report of Rhyacian felsic intrusions in the Minas and Rio das Velhas supergroups of the Quadrilátero Ferrífero;

Rhyacian felsic intrusions in the supracrustal sequences derive from reworked crust;

Rhyacian felsic magmatism around the margins of the Southern São Francisco Craton depicts the collisional stage of the Minas accretionary orogeny.

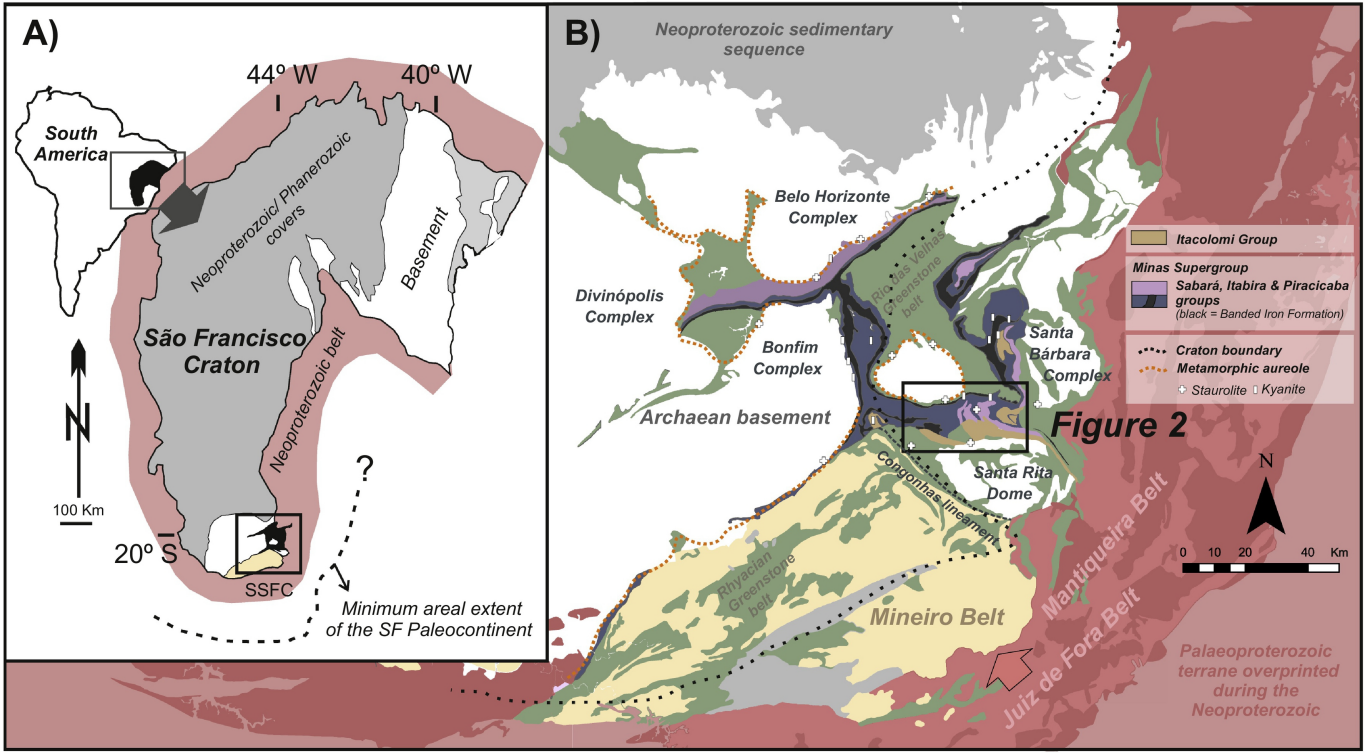
A)
44° W
40° W
South America
Neoproterozoic/ Phanerozoic covers
Basement
São Francisco Craton
Neoproterozoic belt
N
100 Km
20° S
SSFC
?
Minimum areal extent of the SF Paleocontinent
B)
Neoproterozoic sedimentary sequence
Belo Horizonte Complex
Divinópolis Complex
Bonfim Complex
Archaean basement
Rio das Velhas Greenstone belt
Santa Bárbara Complex
Figure 2
Santa Rita Dome
Congonhas lineament
Rhyacian Greenstone belt
Mineiro Belt
Mantiqueira Belt
Juiz de Fora Belt
Palaeoproterozoic terrane overprinted during the Neoproterozoic
Itacolomi Group
Minas Supergroup
Sabará, Itabira & Piracicaba groups
(black = Banded Iron Formation)
Craton boundary
Metamorphic aureole
Staurolite
Kyanite
N
0 10 20 40 Km

Figure 1

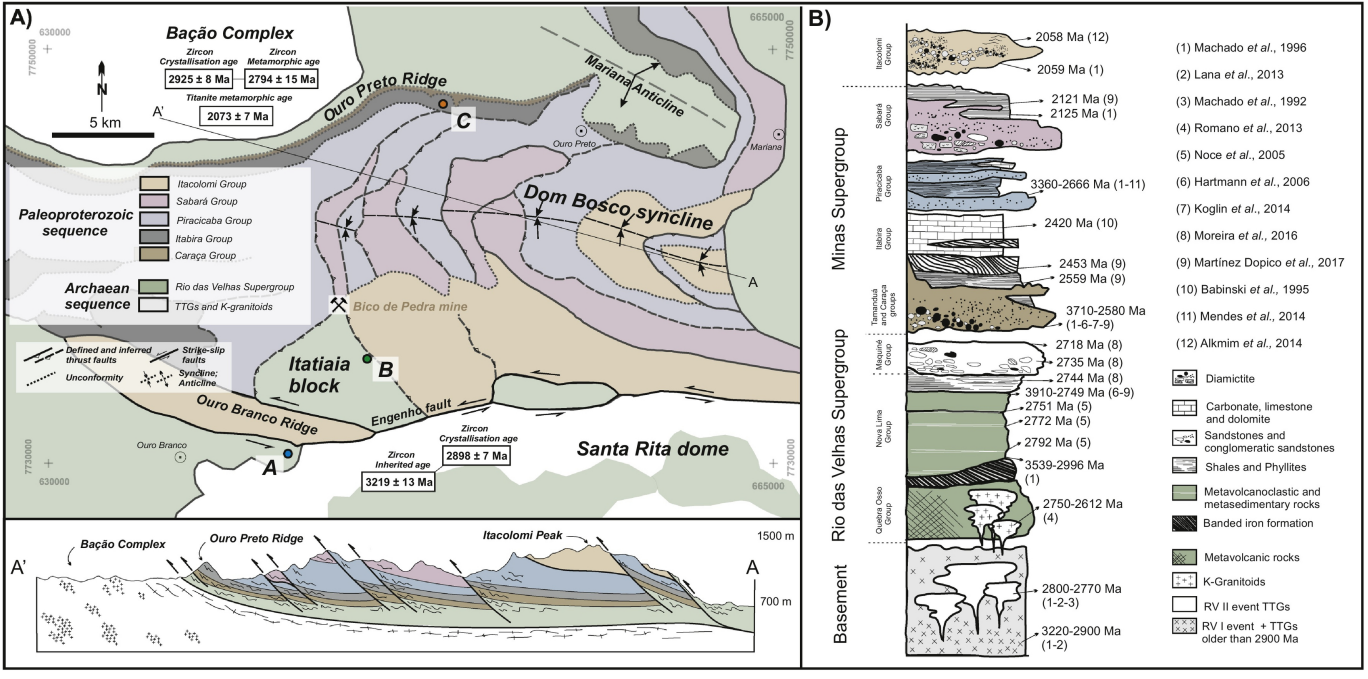
A)
Bação Complex
Zircon Crystallisation age
2925 ± 8 Ma
Zircon Metamorphic age
2794 ± 15 Ma
Titanite metamorphic age
2073 ± 7 Ma
N
5 km
A'
Ouro Preto Ridge
C
Mariana Anticline
Ouro Preto
Mariana
Dom Bosco syncline
A
Paleoproterozoic sequence
Itacolomi Group
Sabará Group
Piracicaba Group
Itabira Group
Caraça Group
Archaean sequence
Rio das Velhas Supergroup
TTGs and K-granitoids
Bico de Pedra mine
Defined and inferred thrust faults
Unconformity
Strike-slip faults
Syncline; Anticline
Itatiaia block
B
Ouro Branco Ridge
Engenho fault
Ouro Branco
A
Zircon Crystallisation age
2898 ± 7 Ma
Zircon Inherited age
3219 ± 13 Ma
Santa Rita dome
630000
7750000
665000
7730000
Bação Complex
Ouro Preto Ridge
Itacolomi Peak
1500 m
700 m
A'
A
B)
2058 Ma (12)
2059 Ma (1)
2121 Ma (9)
2125 Ma (1)
3360-2666 Ma (1-11)
2420 Ma (10)
2453 Ma (9)
2559 Ma (9)
3710-2580 Ma (1-6-7-9)
2718 Ma (8)
2735 Ma (8)
2744 Ma (8)
3910-2749 Ma (6-9)
2751 Ma (5)
2772 Ma (5)
2792 Ma (5)
3539-2996 Ma (1)
2750-2612 Ma (4)
2800-2770 Ma (1-2-3)
3220-2900 Ma (1-2)
Itacolomi Group
Sabará Group
Piracicaba Group
Itabira Group
Tamanduá and Caraça groups
Maquiné Group
Nova Lima Group
Quebra Osso Group
Minas Supergroup
Rio das Velhas Supergroup
Basement
(1) Machado et al., 1996
(2) Lana et al., 2013
(3) Machado et al., 1992
(4) Romano et al., 2013
(5) Noce et al., 2005
(6) Hartmann et al., 2006
(7) Koglin et al., 2014
(8) Moreira et al., 2016
(9) Martínez Dopico et al., 2017
(10) Babinski et al., 1995
(11) Mendes et al., 2014
(12) Alkmim et al., 2014
Diamictite
Carbonate, limestone and dolomite
Sandstones and conglomeratic sandstones
Shales and Phyllites
Metavolcanoclastic and metasedimentary rocks
Banded iron formation
Metavolcanic rocks
K-Granitoids
RV II event TTGs
RV I event + TTGs older than 2900 Ma

Figure 2

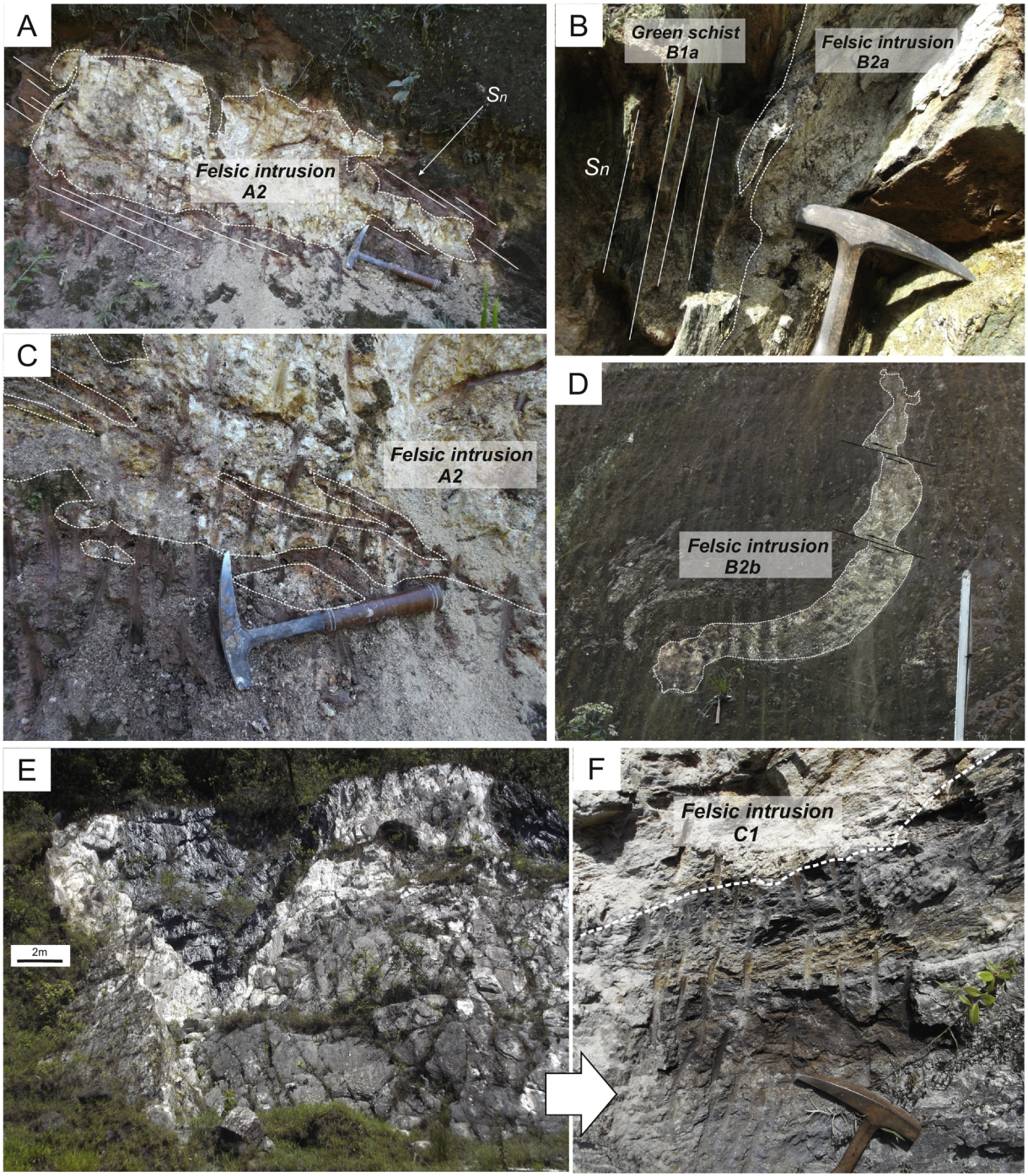
A
Sn
Felsic intrusion
A2
B
Green schist
B1a
Felsic intrusion
B2a
Sn
C
Felsic intrusion
A2
D
Felsic intrusion
B2b
E
2m
F
Felsic intrusion
C1

Figure 3

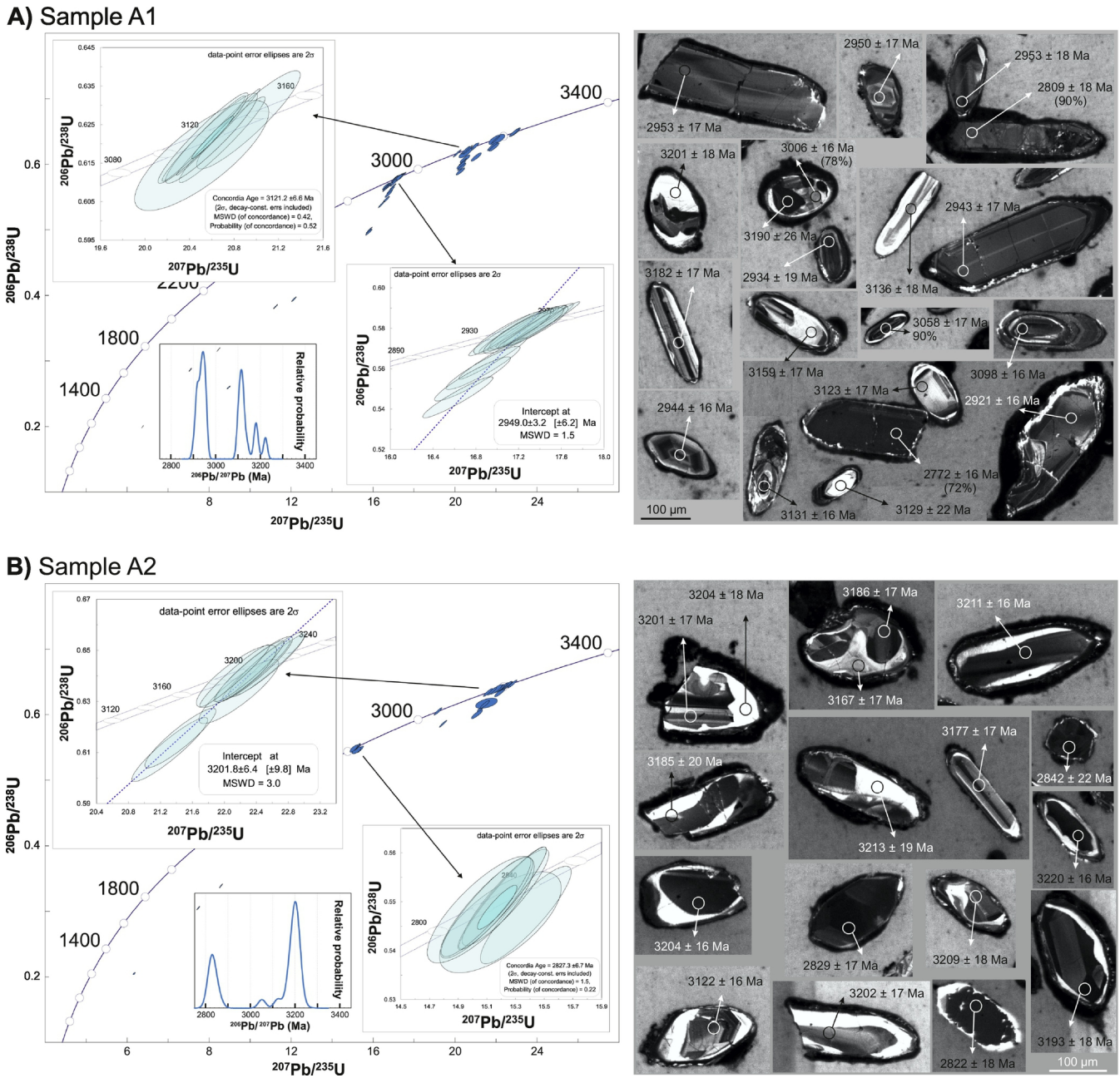
A) Sample A1
data-point error ellipses are 2σ
Concordia Age = 3121.2 ±6.6 Ma
(2σ, decay-const. errs included)
MSWD (of concordance) = 0.42,
Probability (of concordance) = 0.52
Intercept at
2949.0±3.2 [±6.2] Ma
MSWD = 1.5
Relative probability
206Pb/238U
207Pb/235U
206Pb/207Pb (Ma)
2953 ± 17 Ma
2950 ± 17 Ma
2953 ± 18 Ma
2809 ± 18 Ma
(90%)
3201 ± 18 Ma
3006 ± 16 Ma
(78%)
3190 ± 26 Ma
2934 ± 19 Ma
2943 ± 17 Ma
3136 ± 18 Ma
3182 ± 17 Ma
3058 ± 17 Ma
90%
3159 ± 17 Ma
3123 ± 17 Ma
3098 ± 16 Ma
2921 ± 16 Ma
2944 ± 16 Ma
2772 ± 16 Ma
(72%)
3131 ± 16 Ma
3129 ± 22 Ma
100 µm
B) Sample A2
data-point error ellipses are 2σ
Intercept at
3201.8±6.4 [±9.8] Ma
MSWD = 3.0
Concordia Age = 2827.3 ±6.7 Ma
(2σ, decay-const. errs included)
MSWD (of concordance) = 1.5,
Probability (of concordance) = 0.22
Relative probability
206Pb/238U
207Pb/235U
206Pb/207Pb (Ma)
3204 ± 18 Ma
3201 ± 17 Ma
3186 ± 17 Ma
3211 ± 16 Ma
3167 ± 17 Ma
3177 ± 17 Ma
3185 ± 20 Ma
2842 ± 22 Ma
3213 ± 19 Ma
3220 ± 16 Ma
3204 ± 16 Ma
2829 ± 17 Ma
3209 ± 18 Ma
3122 ± 16 Ma
3202 ± 17 Ma
3193 ± 18 Ma
2822 ± 18 Ma
100 µm

Figure 4

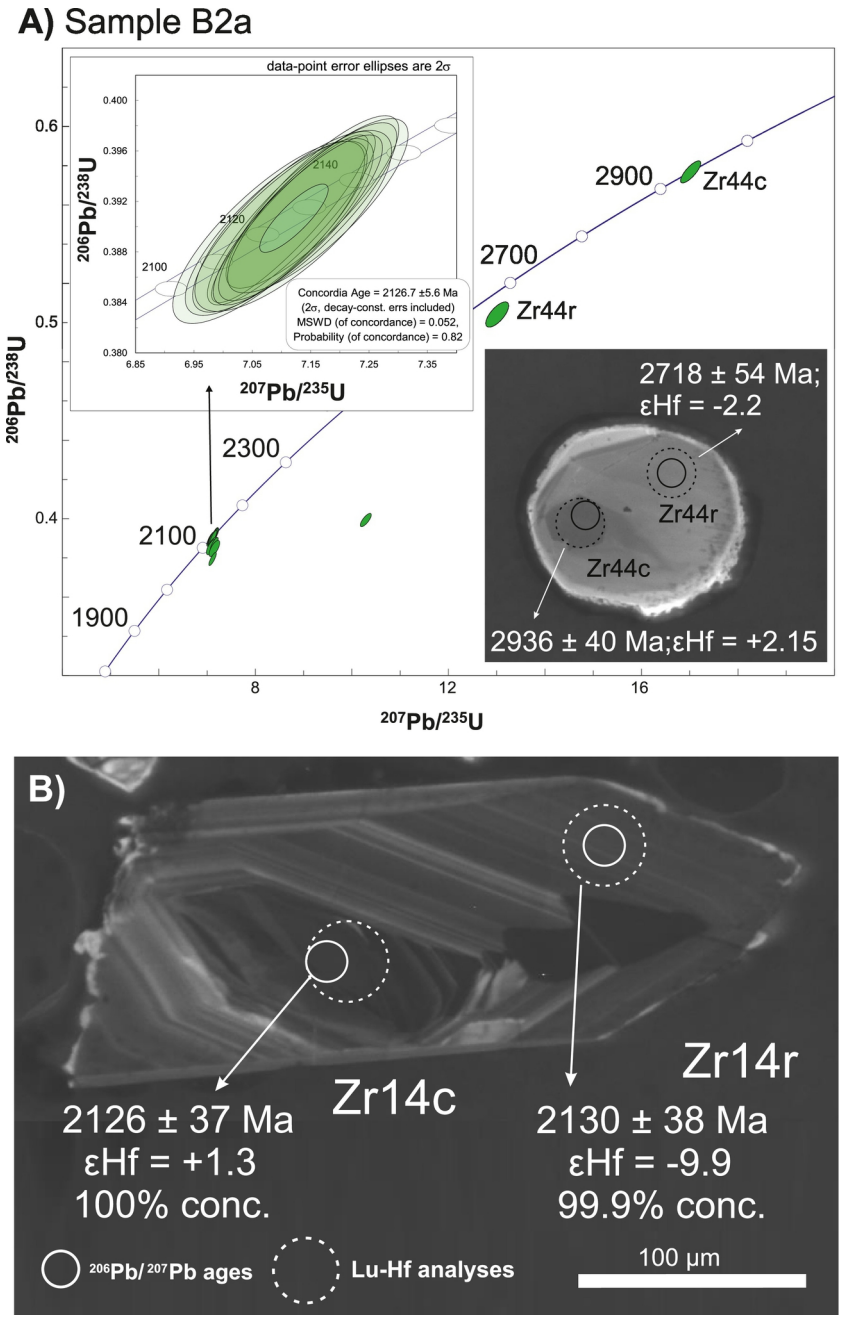
A) Sample B2a
data-point error ellipses are 2σ
Concordia Age = 2126.7 ±5.6 Ma
(2σ, decay-const. errs included)
MSWD (of concordance) = 0.052,
Probability (of concordance) = 0.82
206Pb/238U
207Pb/235U
2718 ± 54 Ma;
εHf = -2.2
Zr44r
Zr44c
2936 ± 40 Ma;εHf = +2.15
2900
2700
2300
2100
1900
B)
Zr14c
Zr14r
2126 ± 37 Ma
εHf = +1.3
100% conc.
2130 ± 38 Ma
εHf = -9.9
99.9% conc.
206Pb/207Pb ages
Lu-Hf analyses
100 µm

Figure 5

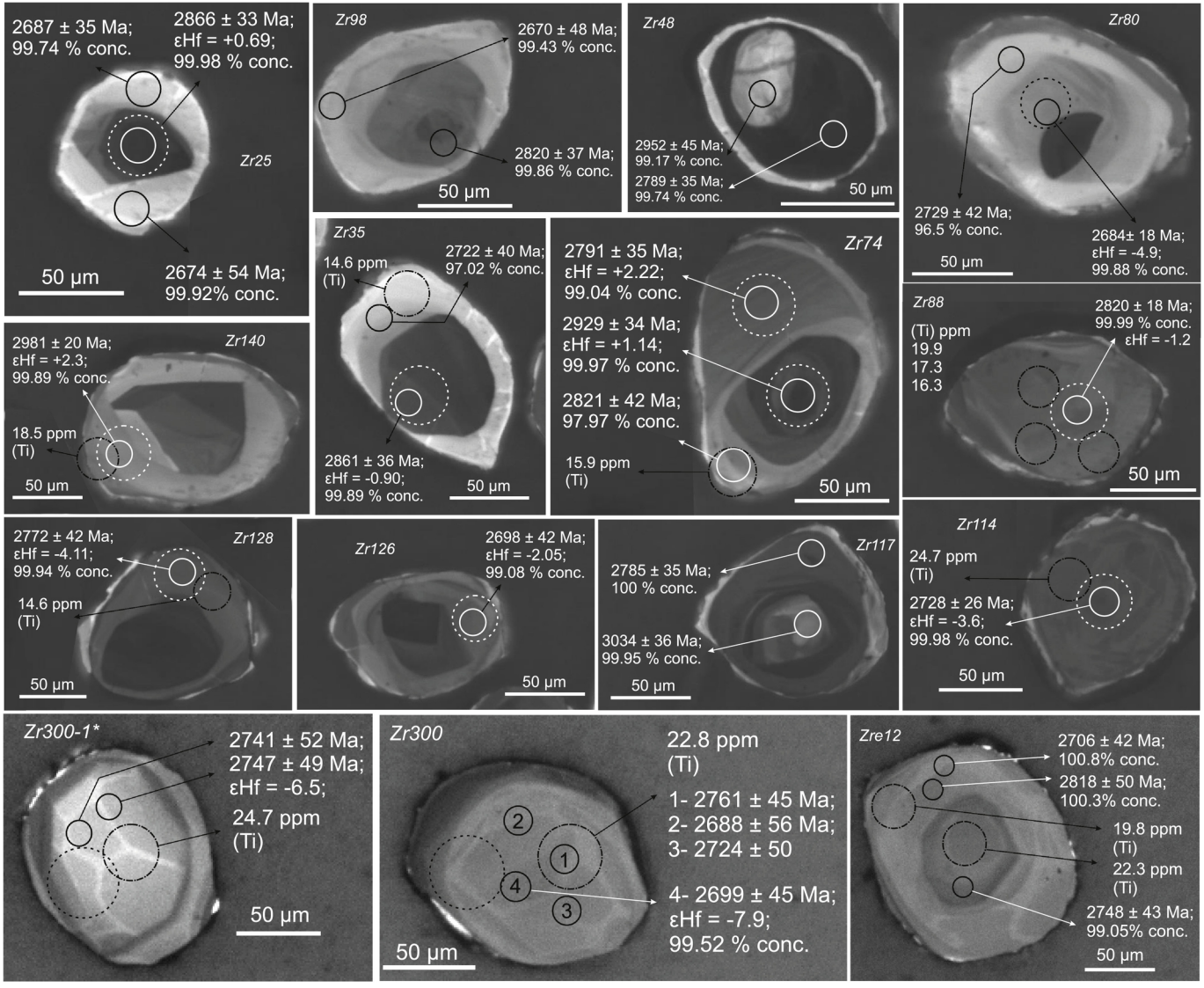
2687 ± 35 Ma;
99.74 % conc.
2866 ± 33 Ma;
εHf = +0.69;
99.98 % conc.
Zr25
50 µm
2674 ± 54 Ma;
99.92% conc.
Zr98
2670 ± 48 Ma;
99.43 % conc.
2820 ± 37 Ma;
99.86 % conc.
50 µm
Zr48
2952 ± 45 Ma;
99.17 % conc.
2789 ± 35 Ma;
99.74 % conc.
50 µm
Zr80
2729 ± 42 Ma;
96.5 % conc.
2684± 18 Ma;
εHf = -4.9;
99.88 % conc.
50 µm
Zr35
14.6 ppm
(Ti)
2722 ± 40 Ma;
97.02 % conc.
2861 ± 36 Ma;
εHf = -0.90;
99.89 % conc.
50 µm
Zr74
2791 ± 35 Ma;
εHf = +2.22;
99.04 % conc.
2929 ± 34 Ma;
εHf = +1.14;
99.97 % conc.
2821 ± 42 Ma;
97.97 % conc.
15.9 ppm
(Ti)
50 µm
Zr88
(Ti) ppm
19.9
17.3
16.3
2820 ± 18 Ma;
99.99 % conc.
εHf = -1.2
50 µm
2981 ± 20 Ma;
εHf = +2.3;
99.89 % conc.
Zr140
18.5 ppm
(Ti)
50 µm
2772 ± 42 Ma;
εHf = -4.11;
99.94 % conc.
Zr128
14.6 ppm
(Ti)
50 µm
Zr126
2698 ± 42 Ma;
εHf = -2.05;
99.08 % conc.
50 µm
Zr117
2785 ± 35 Ma;
100 % conc.
3034 ± 36 Ma;
99.95 % conc.
50 µm
Zr114
24.7 ppm
(Ti)
2728 ± 26 Ma;
εHf = -3.6;
99.98 % conc.
50 µm
Zr300-1*
2741 ± 52 Ma;
2747 ± 49 Ma;
εHf = -6.5;
24.7 ppm
(Ti)
50 µm
Zr300
22.8 ppm
(Ti)
1- 2761 ± 45 Ma;
2- 2688 ± 56 Ma;
3- 2724 ± 50
4- 2699 ± 45 Ma;
εHf = -7.9;
99.52 % conc.
2
1
4
3
50 µm
Zre12
2706 ± 42 Ma;
100.8% conc.
2818 ± 50 Ma;
100.3% conc.
19.8 ppm
(Ti)
22.3 ppm
(Ti)
2748 ± 43 Ma;
99.05% conc.
50 µm

Figure 6

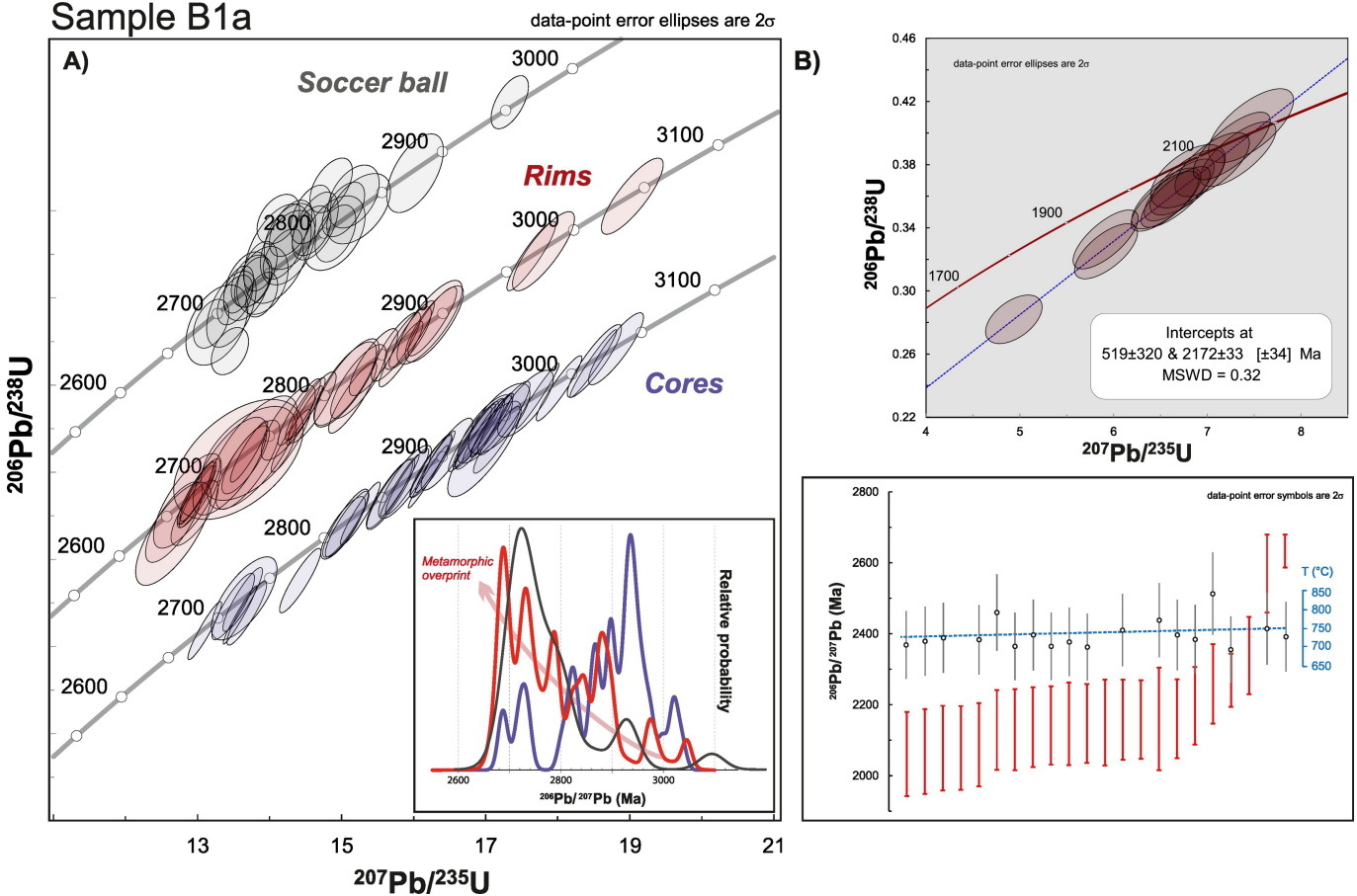
Sample B1a
data-point error ellipses are 2σ
A)
Soccer ball
Rims
Cores
3000
2900
3100
2800
2700
2600
Metamorphic overprint
Relative probability
2600
2800
3000
206Pb/207Pb (Ma)
206Pb/238U
207Pb/235U
13
15
17
19
21
B)
data-point error ellipses are 2σ
2100
1900
1700
0.46
0.42
0.38
0.34
0.30
0.26
0.22
4
5
6
7
8
Intercepts at
519±320 & 2172±33 [±34] Ma
MSWD = 0.32
data-point error symbols are 2σ
T (°C)
850
800
750
700
650
2800
2600
2400
2200
2000

Figure 7

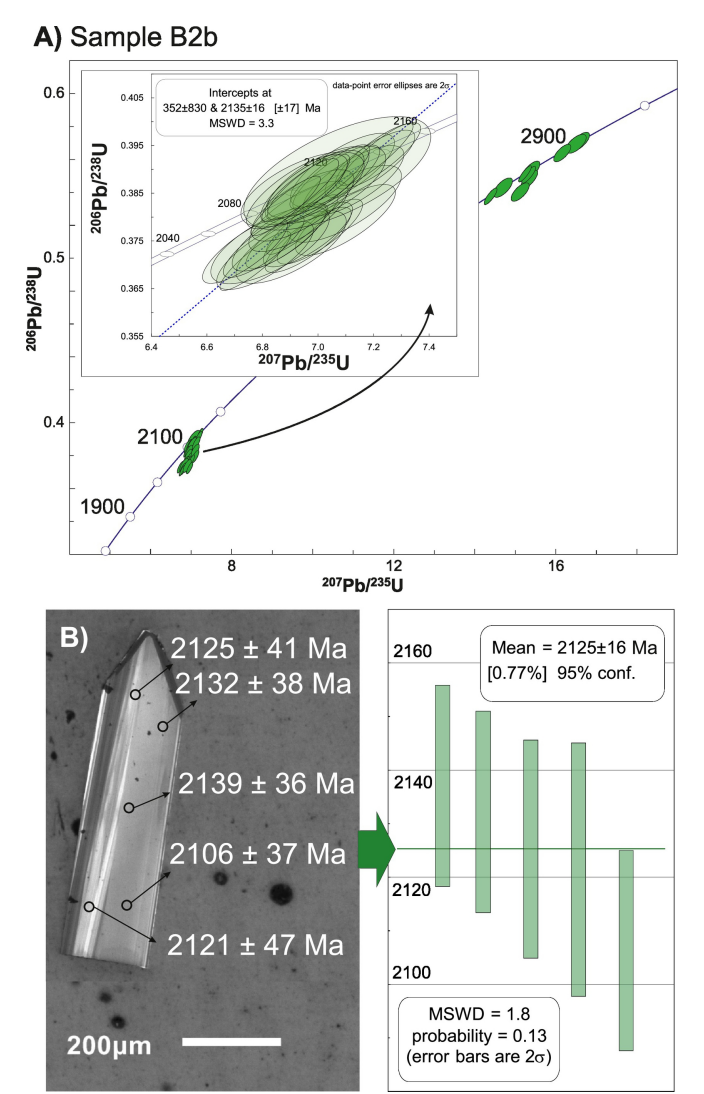
A) Sample B2b
Intercepts at
352±830 & 2135±16 [±17] Ma
MSWD = 3.3
data-point error ellipses are 2σ
2160
2120
2080
2040
2900
2100
1900
206Pb/238U
207Pb/235U
B)
2125 ± 41 Ma
2132 ± 38 Ma
2139 ± 36 Ma
2106 ± 37 Ma
2121 ± 47 Ma
200µm
Mean = 2125±16 Ma
[0.77%] 95% conf.
MSWD = 1.8
probability = 0.13
(error bars are 2σ)

Figure 8

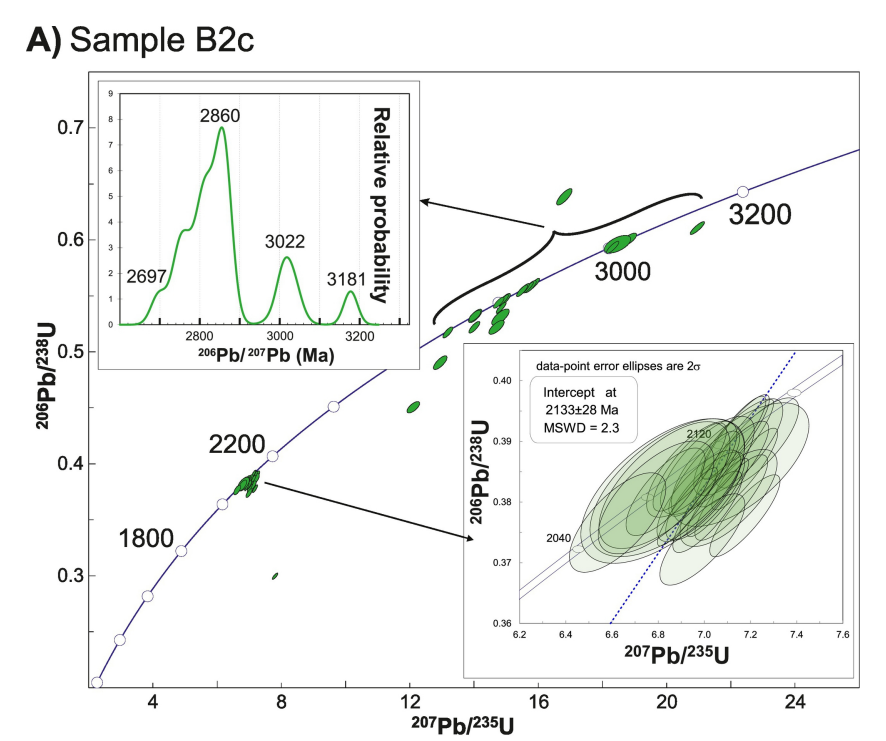
A) Sample B2c
Relative probability
2860
3022
2697
3181
2800
3000
3200
206Pb/207Pb (Ma)
3200
3000
2200
1800
206Pb/238U
207Pb/235U
data-point error ellipses are 2σ
Intercept at
2133±28 Ma
MSWD = 2.3
2120
2040
6.2
6.4
6.6
6.8
7.0
7.2
7.4
7.6
0.36
0.37
0.38
0.39
0.40

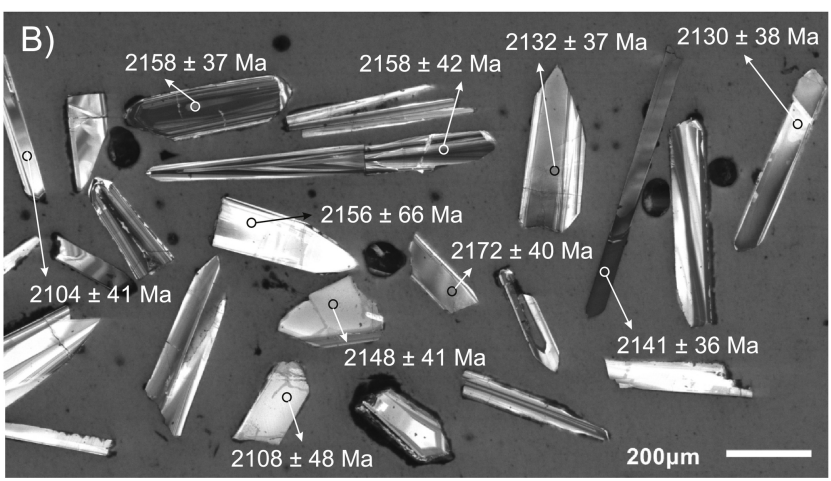
B)
2158 ± 37 Ma
2158 ± 42 Ma
2132 ± 37 Ma
2130 ± 38 Ma
2156 ± 66 Ma
2172 ± 40 Ma
2104 ± 41 Ma
2148 ± 41 Ma
2141 ± 36 Ma
2108 ± 48 Ma
200µm

Figure 9

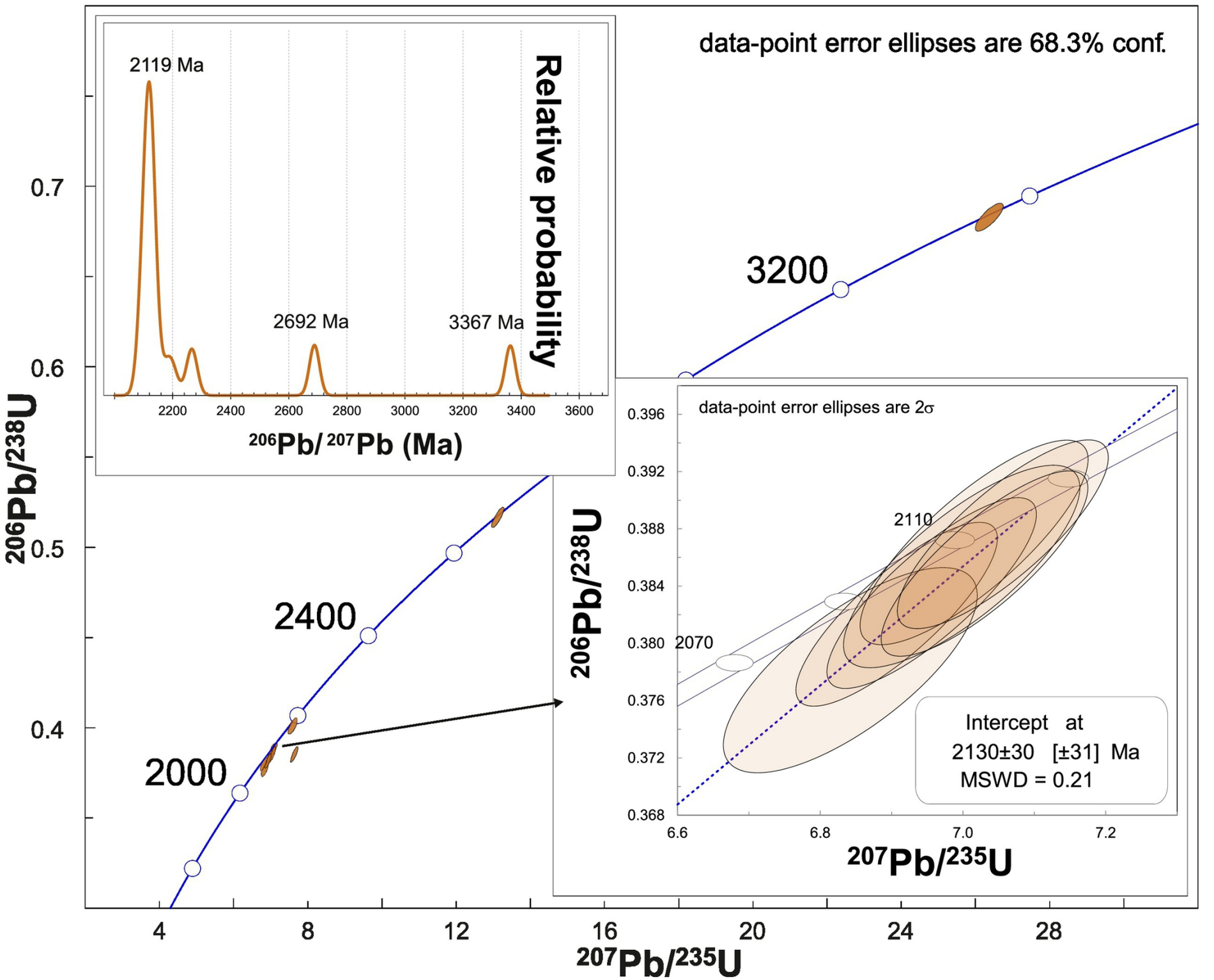
Sample C1
data-point error ellipses are 68.3% conf.
2119 Ma
2692 Ma
3367 Ma
Relative probability
206Pb/207Pb (Ma)
3200
2400
2000
206Pb/238U
207Pb/235U
data-point error ellipses are 2σ
2110
2070
Intercept at
2130±30 [±31] Ma
MSWD = 0.21

Figure 10

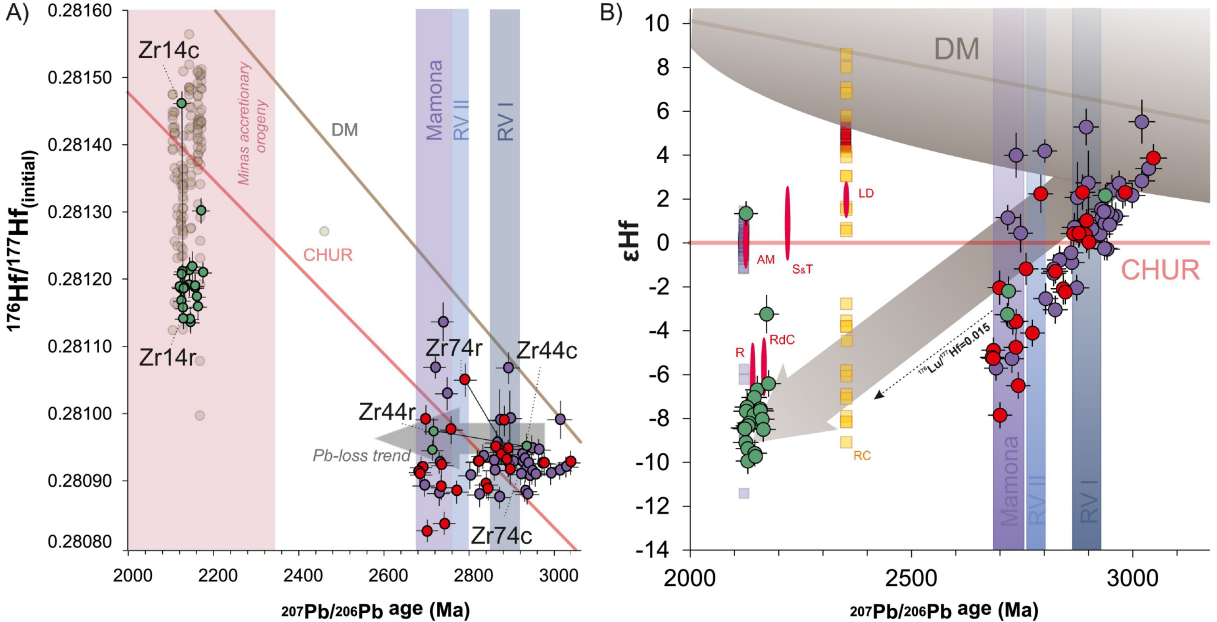
A)
Zr14c
Zr14r
Minas accretionary orogeny
DM
CHUR
Mamona
RV II
RV I
Zr74r
Zr44c
Zr44r
Pb-loss trend
Zr74c
176Hf/177Hf(initial)
207Pb/206Pb age (Ma)
B)
DM
LD
AM
SaT
CHUR
R
RdC
RC
176Lu/177Hf=0.015
Mamona
RV II
RV I
εHf
207Pb/206Pb age (Ma)

Figure 11

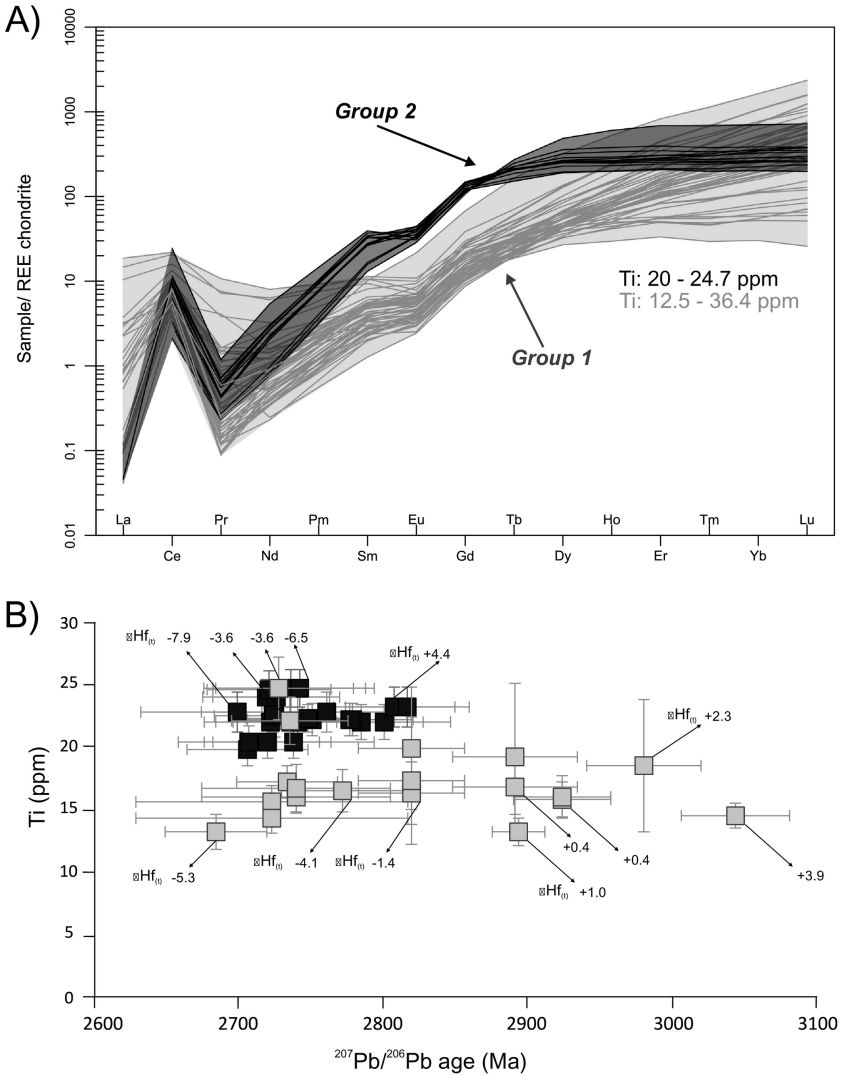
A)
Sample/ REE chondrite
10000
1000
100
10
1
0.1
0.01
Group 2
Group 1
Ti: 20 - 24.7 ppm
Ti: 12.5 - 36.4 ppm
La
Ce
Pr
Nd
Pm
Sm
Eu
Gd
Tb
Dy
Ho
Er
Tm
Yb
Lu
B)
Ti (ppm)
30
25
20
15
10
5
0
εHf(t) -7.9
-3.6
-3.6
-6.5
εHf(t) +4.4
εHf(t) +2.3
+0.4
+0.4
+3.9
εHf(t) -5.3
εHf(t) -4.1
εHf(t) -1.4
εHf(t) +1.0
2600
2700
2800
2900
3000
3100
207Pb/206Pb age (Ma)

Figure 12